

Deep Learning to Automate Parameter Extraction and Model Fitting of Two-Dimensional Transistors

Robert K. A. Bennett,¹ Jan-Lucas Uslu,^{2,3} Harmon F. Gault,¹ Asir Intisar Khan,¹ Lauren Hoang,¹ Tara Peña,¹ Kathryn Neilson,¹ Young Suh Song,¹ Zhepeng Zhang,^{3,4} Andrew J. Mannix,^{3,4} Eric Pop^{1,3,4,5,*}

¹Department of Electrical Engineering, Stanford University, Stanford, CA 94305, USA

²Department of Physics, Stanford University, Stanford, CA 94305, USA

³Stanford Institute for Materials and Energy Sciences, SLAC National Accelerator Laboratory, Menlo Park, CA 94025, USA

⁴Department of Materials Science and Engineering, Stanford University, Stanford, CA 94305, USA

⁵Department of Applied Physics, Stanford University, Stanford, CA 94305, USA

*Contact: epop@stanford.edu

Abstract

We present a deep learning approach to extract physical parameters (e.g., mobility, Schottky contact barrier height, defect profiles) of two-dimensional (2D) transistors from electrical measurements, enabling automated parameter extraction and technology computer-aided design (TCAD) fitting. To facilitate this task, we implement a simple data augmentation and pre-training approach by training a secondary neural network to approximate a physics-based device simulator. This method enables high-quality fits after training the neural network on electrical data generated from physics-based simulations of ~ 500 devices, a factor $>40\times$ fewer than other recent efforts. Consequently, fitting can be achieved by training on physically rigorous TCAD models, including complex geometry, self-consistent transport, and electrostatic effects, and is not limited to computationally inexpensive compact models. We apply our approach to reverse-engineer key parameters from experimental monolayer WS_2 transistors, achieving a median coefficient of determination (R^2) = 0.99 when fitting measured electrical data. We also demonstrate that this approach generalizes and scales well by reverse-engineering electrical data on high-electron-mobility transistors while fitting 35 parameters simultaneously. To facilitate future research on deep learning approaches for inverse transistor design, we have published our code and sample data sets online.

Introduction

Emerging semiconductors, such as two-dimensional (2D) transition metal dichalcogenides (TMDs),¹ amorphous oxides,² and carbon nanotubes,³ show great promise to enable next-generation electronic devices. Field-effect transistors (FETs) based on these materials are frequently characterized by fitting their measured electrical characteristics to models that express current in terms of either material-level parameters (e.g., semiconductor mobility, Schottky contact barrier height) or device-level parameters (e.g., lumped contact resistances or parasitic capacitances). An advantage of this *model fitting* approach is that it simultaneously extracts multiple relevant quantities from a few measurements while enabling follow-up simulations to assess performance limitations or circuit-level analyses. However, fitting models to measured data tends to be an iterative process, even for experts in device simulations, making this powerful characterization tool both time-consuming and inaccessible to many researchers.⁴

To address these limitations, recent studies have developed neural networks that can predict model parameters from current *vs.* gate-to-source voltage and/or capacitance *vs.* gate-to-source voltage characteristics, achieving excellent fits after training these models on simulated data from 20,000 – 1,000,000 unique devices.⁵⁻¹⁰

Acquiring such large training sets is easy for established technologies with computationally inexpensive models: for example, established compact models for gallium nitride¹¹ or silicon¹² transistors can compute hundreds or thousands of simulated electrical measurements per second. However, emerging FETs are frequently modeled using computationally expensive simulations¹³⁻¹⁵ – often because the physics of such devices is more difficult to approximate, or because model development has lagged behind mature technologies – and can require minutes to hours^{16,17} to generate a single current vs. voltage curve. For this reason, acquiring large data sets for training and fitting emerging device behavior is often intractable.

In this work, we develop a deep learning approach for FET parameter extraction that requires significantly less training data compared to other recent efforts. We reduce the amount of expensive training data by implementing a secondary surrogate network to approximate the electrical model, which we use to generate a large (and computationally inexpensive) augmented data set that we use to pre-train our primary network. Afterwards, we fine tune the primary network using data generated by the original physics-based model. This approach, from start to finish, requires generating electrical data from only ~ 500 devices ($>40\times$ fewer compared to previous works) to achieve excellent reverse-engineered fits to experimental data.

We verify our approach using both simulated and experimental test sets, obtaining median coefficients of determination (R^2) fits of 0.995 and 0.990, respectively, when fitting eight model parameters. We further demonstrate that our approach works for other types of FETs and scales well as the electrical models become more complex (i.e., have more fitting parameters). To facilitate future research, we have also published our data sets and machine learning code (implemented in Python using TensorFlow¹⁸) in a GitHub repository.¹⁹

Overview of the deep learning approach

In a standard electrical modeling task, the user inputs a set of model parameters, Y_{given} (e.g., carrier mobility, Schottky contact barrier height, etc.), into a *forward model*, M_{forward} , to compute a current I_{modeled} :

$$M_{\text{forward}}(Y_{\text{given}}) = I_{\text{modeled}} \quad (1)$$

Here, we aim to train a neural network for the inverse problem.²⁰ That is, given the measured current I_{measured} , we aim to train a neural network N_{inverse} to predict the set of parameters $Y_{\text{predicted}}$:

$$N_{\text{inverse}}(I_{\text{measured}}) = Y_{\text{predicted}} \quad (2)$$

such that our original forward model reproduces the measured current:

$$I_{\text{measured}} \approx M_{\text{forward}}[N_{\text{inverse}}(I_{\text{measured}})] = I_{\text{modeled}} \quad (3)$$

Our approach for accomplishing this task is summarized in **Figure 1** and below:

1. Use a comprehensive physics-based model (e.g., Sentaurus Device²¹) to generate a training data set of input parameters and calculated electrical characteristics (**Figure 1a**).
2. Train an intermediate forward neural network to approximate the physics-based model (**Figure 1b**).

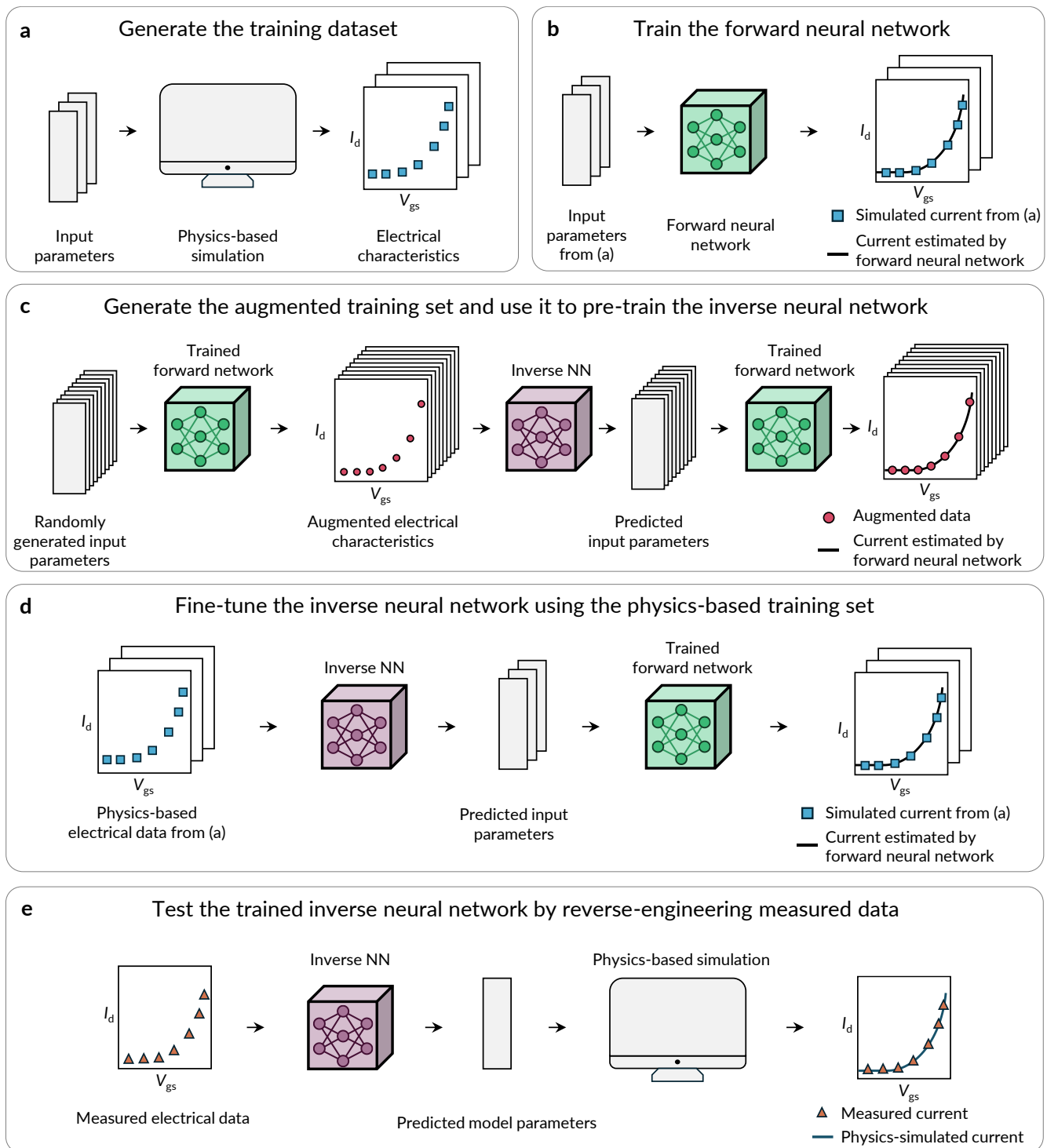


Figure 1: Overview of our deep learning approach for reverse-engineering FET model parameters. We begin by (a) generating a training set of model input parameters and output electrical characteristics from a physics-based device simulator (here, we use Sentaurus Device). (b) We then train a forward neural network to reproduce the data from the physics-based simulator and (c) use this forward network to generate an augmented data set with which we pre-train the inverse neural network, then we finish training on the original physics-simulated electrical data (d). In (c) and (d), we train the inverse neural network to predict model parameters that will reproduce the original input current; we estimate the current during training by calling the pre-trained forward neural network from step (b) to do so (i.e., as a tandem neural network). (e) Next, we test the trained inverse neural network by providing it with experimental electrical data to be reverse-engineered, extracting the model parameters, and running new physics-based simulations using the predicted parameters. Finally, we plot the new simulated curves alongside the original measured data to assess the quality of the fit.

3. Generate a much larger augmented training set using the forward neural network and use this augmented data to pre-train the inverse neural network, calling the forward neural network repeatedly to guide training as a *tandem neural network* (**Figure 1c**).²²
4. Finish training the inverse neural network using the original data set from step 1, once again calling the forward neural network repeatedly to guide training as a tandem neural network (**Figure 1d**).
5. Test the inverse neural network by inputting new electrical data, extracting the model parameters, and calling the physics-based model on the predicted model parameters to assess the accuracy of the extraction (**Figure 1e**).

Generating the training set with a physics-based simulator

We generate our training data using Sentaurus Device,²¹ an industry-standard technology computer-aided design (TCAD) program, as our physics-based model. This simulator can be any software that generates complete current *vs.* gate-to-source voltage data based on physical input parameters such as device geometry and material properties; other examples include Monte Carlo²³ or quantum transport simulators.^{14,15} For any fit to provide valid physical insights, regardless of how the fit is achieved – through conventional techniques or otherwise – the user must take care to ensure that the model used to generate the training data accurately describes their transistors. For instance, with enough fitting parameters, many models could allow for a close fit between measured and modeled data, even if the physics of the model are wrong, oversimplified, or irrelevant. However, for some applications, this could also be acceptable: for instance, empirical “phenomenological” models²⁴ and surrogate models²⁵ can be practical for circuit-level SPICE²⁶ simulations.

In our work, we use Sentaurus Device to generate I_d - V_{gs} curves (where I_d is the drain current and V_{gs} is the gate-to-source voltage) for 2D FETs using the device geometry shown in **Figure 2a**. This *back-gated* geometry is frequently used in experimental studies on 2D or other emerging semiconductors because it is easier to fabricate than top- or dual-gated devices; we use this structure here because we test our neural networks on readily available experimental I_d - V_{gs} data from monolayer semiconductor transistors. We include additional Sentaurus Device simulation details in **Supplementary Section 1**.

To build our training set, we initialize n -type FETs in Sentaurus Device TCAD²¹ with the geometry shown in **Figure 2a**, choosing the value of each model parameter at random from the ranges listed in **Table I**. Here, we intentionally use large ranges for each parameter to ensure the neural network can fit a wide range of device data, as the neural network cannot predict the values of parameters outside of these ranges. We justify these chosen ranges in **Supplementary Section 2**. With this approach, we then simulate sets of I_d - V_{gs} characteristics for 25,000 devices from $V_{gs} = -6$ to 50 V at $V_{ds} = 0.1$ and 1.0 V, creating a large set of established I_d - V_{gs} *vs.* model input parameter relationships with which we train our neural networks. We will later use subsets of this larger training set in bootstrap studies to determine the minimum acceptable training set size.

Parameter	Range	Unit
Mobility	1 – 35	$\text{cm}^2 \text{V}^{-1} \text{s}^{-1}$
Schottky contact barrier height	10 – 510	meV
Effective density of states N_C	$2 \times 10^{11} - 9 \times 10^{12}$	cm^{-2}
Peak donor density N_{D0}	$3 \times 10^{12} - 3 \times 10^{13}$	$\text{eV}^{-1} \text{cm}^{-2}$
Donor energy mid $E_{D,\text{mid}}$	20 – 200	meV below E_C
Donor energy width σ_D	20 – 200	meV
Peak acceptor band tail density N_{A0}	$6 \times 10^{11} - 3.7 \times 10^{13}$	$\text{eV}^{-1} \text{cm}^{-2}$
Acceptor band tail energy width σ_A	50 – 300	meV

Table I: Model parameters and the ranges across which they vary in the physics-based training set. N_{D0} , $E_{D,\text{mid}}$, and σ_D characterize donor-like defects, and N_{A0} and σ_A characterize acceptor-like band-tail states. The defect-like and acceptor-like profiles are shown in **Figures 2b,c**, respectively. We elaborate upon the physical origin and/or meaning of these parameters and justify these selected ranges in **Supplementary Section 2**.

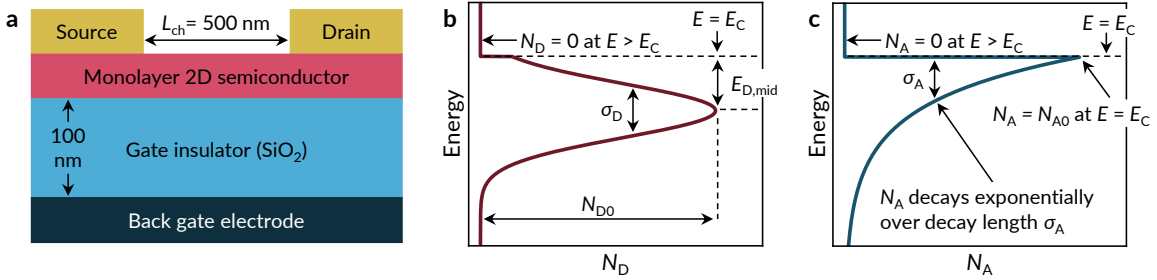


Figure 2: Summary of transistors considered in this work. (a) Diagram of our transistor geometry, showing a two-dimensional semiconductor integrated into back-gated field-effect transistor (not to scale). (b) The donor-like defect profile N_D and (c) the acceptor-like band-tail N_A . These profiles are given in **Eqs. (4) and (5)**, respectively, and are parameterized in terms of the model parameters listed in **Table I**.

Model parameters for two-dimensional transistors

The parameters we aim to fit include the electron mobility μ , Schottky contact barrier height ϕ_B , and effective density of states at the conduction band edge N_C . These parameters capture, respectively, the speed at which electrons can move through a semiconductor, the energy barrier associated with electron injection between the semiconductor and metal, and the number of available states for electrons in the semiconductor. The remaining parameters quantify defect profiles in 2D devices. Donor states (e.g., chalcogen vacancies; see **Supplementary Section 2**) follow a truncated Gaussian distribution (**Figure 2b**) with respect to energy E ,

$$N_D(E) = N_{D0} \exp\left(-\frac{(E-E_{D,\text{mid}})^2}{2\sigma_D^2}\right) \text{ for } E < E_C \quad N_D(E) = 0 \text{ otherwise} \quad (4)$$

where N_{D0} is the peak donor density, $E_{D,\text{mid}}$ is the energy at which the Gaussian donor distribution peaks (referenced to the conduction band edge E_C), and σ_D is the standard deviation (width) of the Gaussian curve.

We also include trap-like acceptor states (**Figure 2c**), which could arise from dispersionless band-tail states (see **Supplementary Section 2**). Their distribution decays exponentially from the conduction band edge E_C :

$$N_A(E) = N_{A0} \exp\left(-\left|\frac{E-E_C}{\sigma_A}\right|\right) \text{ for } E < E_C \quad N_A(E) = 0 \text{ otherwise} \quad (5)$$

where N_{A0} is the peak acceptor density and σ_A is the characteristic decay energy. We elaborate upon the physical meaning of each fitting parameter in **Supplementary Section 2**.

Training the inverse neural network in tandem with a forward solver

The inverse neural network architecture used in this work is shown in **Figure 3a**. This neural network accepts I_d - V_{gs} data from physics-based simulations ($V_{ds} = 0.1$ and 1.0 V, with 32 V_{gs} values evenly spaced from -6 to $+50$ V); we also perform simple feature engineering by explicitly inputting $\partial I_d/\partial V_{gs}$, $\log_{10}(I_d)$, and $\partial \log_{10} I_d/\partial V_{gs}$ for each V_{ds} , yielding 8 vectors that we input into the neural network as a 32×8 matrix. We discuss and justify this feature engineering in **Supplementary Section 3**. Other recent works on machine learning-based parameter extraction have also included capacitance-voltage data as input features for silicon-based devices.⁹ Although including such data would likely facilitate training and fitting, these capacitances are not consistently measured for 2D devices today, unlike I_d - V_{gs} characteristics. To ensure our approach remains applicable to experimental 2D transistors without demanding additional measurements, we avoid relying upon these capacitance measurements here.

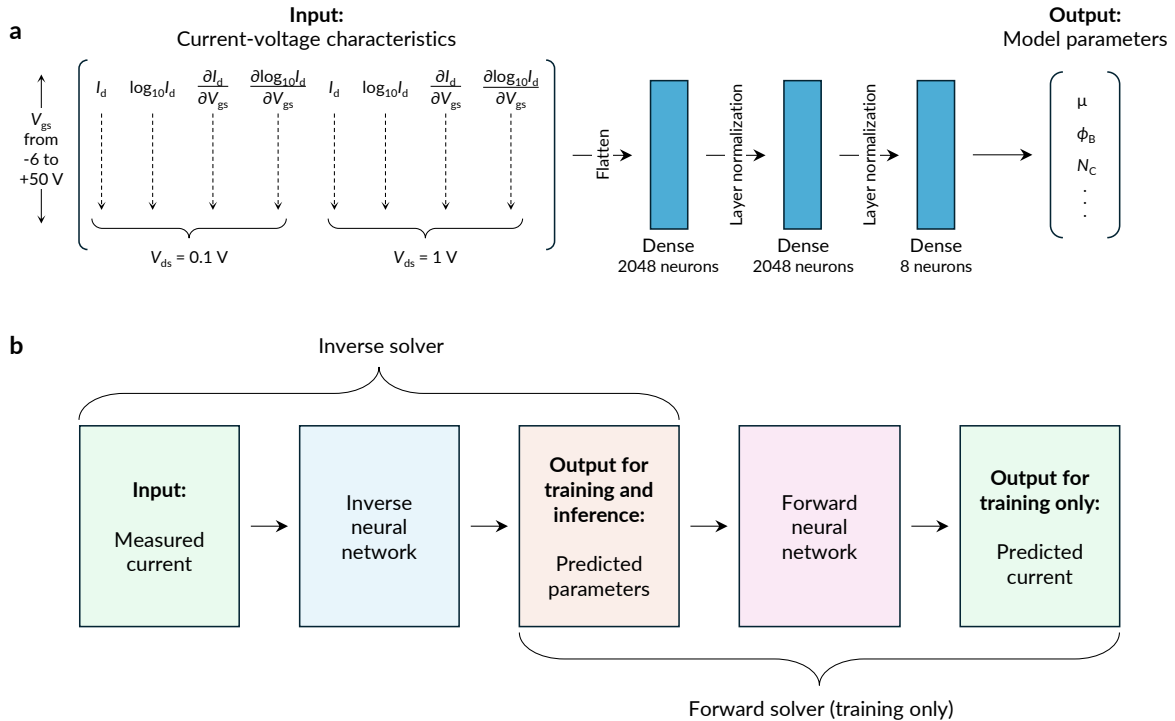


Figure 3: Inverse neural network and tandem network training approach. (a) Architecture of the inverse neural network used in this work. Each dense layer uses the rectified linear unit (ReLU) activation function, except the final layer, which uses the hyperbolic tangent (tanh) activation function. The network accepts current vs. gate-to-source voltage (I_d - V_{gs}) measurements in linear and logarithmic space, along with their derivatives with respect to V_{gs} , and outputs the set of model parameters that a physics-based solver can use to reproduce this input data. (b) The tandem approach used for training the inverse neural network. During training, the parameters that the network outputs are fed into a pre-trained forward neural network, which allows us to include errors of predicted current in the loss function. We use this tandem approach only while training; during inference, the network outputs the predicted parameters directly. Details of the training procedures and of the forward neural network are given in **Supplementary Sections 4 and 5**.

The inverse neural network aims to output the set of Sentaurus model parameters associated with these I_d - V_{gs} curves and derivatives. To accomplish this, we use the *tandem neural network* approach summarized in **Figure 3b**. Such tandem neural networks have found widespread use in many inverse design tasks,^{22,27,28} including transistor parameter extraction.⁷ In this approach, the inverse neural network is trained by feeding its output (i.e., the Sentaurus Device model parameters) into a pre-trained forward neural network, which then outputs the estimated I_d - V_{gs} characteristics corresponding to those model parameters. In other words, the forward neural network approximates the original physics-based TCAD solver or, equivalently, it approximates $\mathbf{M}_{\text{forward}}$ in **Eq. (1)**. We describe all scaling, preprocessing, and training procedures in **Supplementary Section 4**, and we characterize the forward neural network in **Supplementary Section 5**.

A tandem approach is necessary here because I_d - V_{gs} characteristics are generally not unique functions of the model parameters.⁷ In other words, there are often multiple sets of input parameters that can allow the physics-based simulator to yield identical or near-identical I_d profiles, making it difficult to train the inverse neural network based on errors in parameters alone. Instead, training the inverse neural network using a tandem approach allows us to incorporate errors in both parameters and predicted current into the loss function:

$$\mathcal{L} = \left(\frac{1}{N_{\text{devices}}}\right) \left(\frac{1}{N_{\text{params}}}\right) \sqrt{\sum_i^{N_{\text{devices}}} \sum_{\ell}^{N_{\text{params}}} \left(Y_{\text{actual}}^{(i,\ell)} - Y_{\text{pred}}^{(i,\ell)}\right) E_{I_d}^{(i)}} \quad (6)$$

where N_{devices} is the number of devices, N_{params} is the number of fitting parameters in the parameter set Y , the subscripts ‘‘actual’’ and ‘‘pred’’ denote baseline truths and predicted quantities, and the superscripts (i) and (ℓ) denote the i^{th} device and ℓ^{th} fitting parameter, respectively. $E_{I_d}^{(i)}$ is the error in I_d between the actual and predicted currents and their derivatives, given by **Supplementary Eq. (S1)** in **Supplementary Section 4**. During training, we estimate the predicted current $I_{\text{predicted}}^{(i)}$ by calling the forward network on the predicted parameter set, i.e., $I_{\text{predicted}}^{(i)} = \mathbf{M}_{\text{forward}}(Y_{\text{pred}}^{(i)})$.

We emphasize that we use this tandem approach only for *training* the inverse neural network, not for inference.

Pre-training with an augmented data set and fine-tuning with physics-based data

We take advantage of the forward neural network to build an augmented data set that we use to pre-train our inverse network. Here, we generate many sets of randomly chosen input parameters using the same parameters and ranges from **Table I**, then use the forward network to estimate the corresponding I_d - V_{gs} curves. These augmented data are essentially free compared to our original physics-based simulated data: it takes ~ 1 minute to generate a single I_d - V_{gs} curve with Sentaurus (for other device simulators, this time can vary greatly, depending on the specific device and models used), whereas we can generate 100,000 I_d - V_{gs} curves with the forward neural network in less than 30 seconds. After pre-training our inverse neural network on this augmented data set, we use the physics-based simulation training set to fine-tune the model. We detail full training procedures in **Supplementary Section 4**.

After training, we test the performance of the inverse neural network by using it to extract estimated model parameters from a Sentaurus Device-simulated test of 1,000 devices (generated with the same procedure as training and development sets) that were unseen by the neural network during training and network optimization. Afterwards, we take these extracted parameters and estimate their corresponding I_d - V_{gs} curves using a well-trained forward neural network that was trained on all 25,000 devices in our original physics-based training set. We show in **Supplementary Section S5** that this forward neural network reproduces our original Sentaurus simulations with exceptional accuracy; thus, this approach allows us to estimate the accuracy of the inverse neural network without having to re-run Sentaurus Device simulations, which can become computationally expensive when repeatedly evaluating the performance of the inverse neural network on multiple training sizes. Finally, we calculate R^2 between the original and newly obtained I_d - V_{gs} characteristics to quantify how accurately these estimated parameters can reproduce the original I_d - V_{gs} curves (higher R^2 is better; $R^2 = 1$ denotes a perfect fit; details of the R^2 calculation are described in **Supplementary Section 4**).

Our original physics-based training set contains I_d - V_{gs} curves from 25,000 unique devices; however, we wish to develop a machine learning approach that relies upon as few simulations as possible, since they are computationally expensive. Thus, we apply the bootstrap approach described in **Supplementary Section 4** to draw smaller training sets to quantify how the training set size impacts the performance of the neural network. Note that when we refer to the training set size, we refer to the number of device configurations used for physics-based simulations in both the training and development sets combined and that for each bootstrapped training procedure, we use the same subset of data to train both the forward and inverse networks. For example, if we specify that the training set size is 500, we (i) use 500 sets of physics-based simulations to train the forward neural network; (ii) use that forward neural network to generate a large augmented data set (100,000 sets of I_d - V_{gs} curves) with which we train the inverse neural network; and then (iii) fine-tune the inverse neural network on the original 500 physics-based simulations.

We plot the 5th quantile (worst 5%) R^2 for various training set sizes, with and without pre-training, in **Figures 4a**, and show sample histograms for training sets consisting of 500 and 1,000 devices in **Figure 4b**. Here, we find that pre-training significantly improves the performance of the inverse neural network; in terms of R^2 fit, implementing this pre-training procedure appears to offer an accuracy boost roughly equivalent to doubling the size of the original physics-based training set. We show sample fits corresponding to the 5th quantile (worst 5%), 10th quantile (worst 10%), and median R^2 in **Figures 4c-e** for an inverse neural network with pre-training (500 devices in the physics-based training set), confirming a good match between the original simulated I_d - V_{gs} data and that obtained with the reverse-engineered parameters.

Our approach sharply reduces the number of physics-based (Sentaurus Device TCAD) simulations needed to achieve excellent fits across the majority of the test set compared to previous studies. These past efforts have used training sets consisting of 20,000 – 1,000,000 devices to achieve high-quality fits for a similar reverse-engineering task, whereas we demonstrate excellent fits using training sets of \sim 500 devices, reducing the required number of training devices by \sim 40 \times . For this training set size, the full training procedure takes less than five minutes (including training the forward network, generating the augmented data set, and then pre-

training and fine tuning the inverse neural network) on an NVIDIA RTX 4080 graphics processing unit, which is much less time compared to that required to generate the physics-based data.

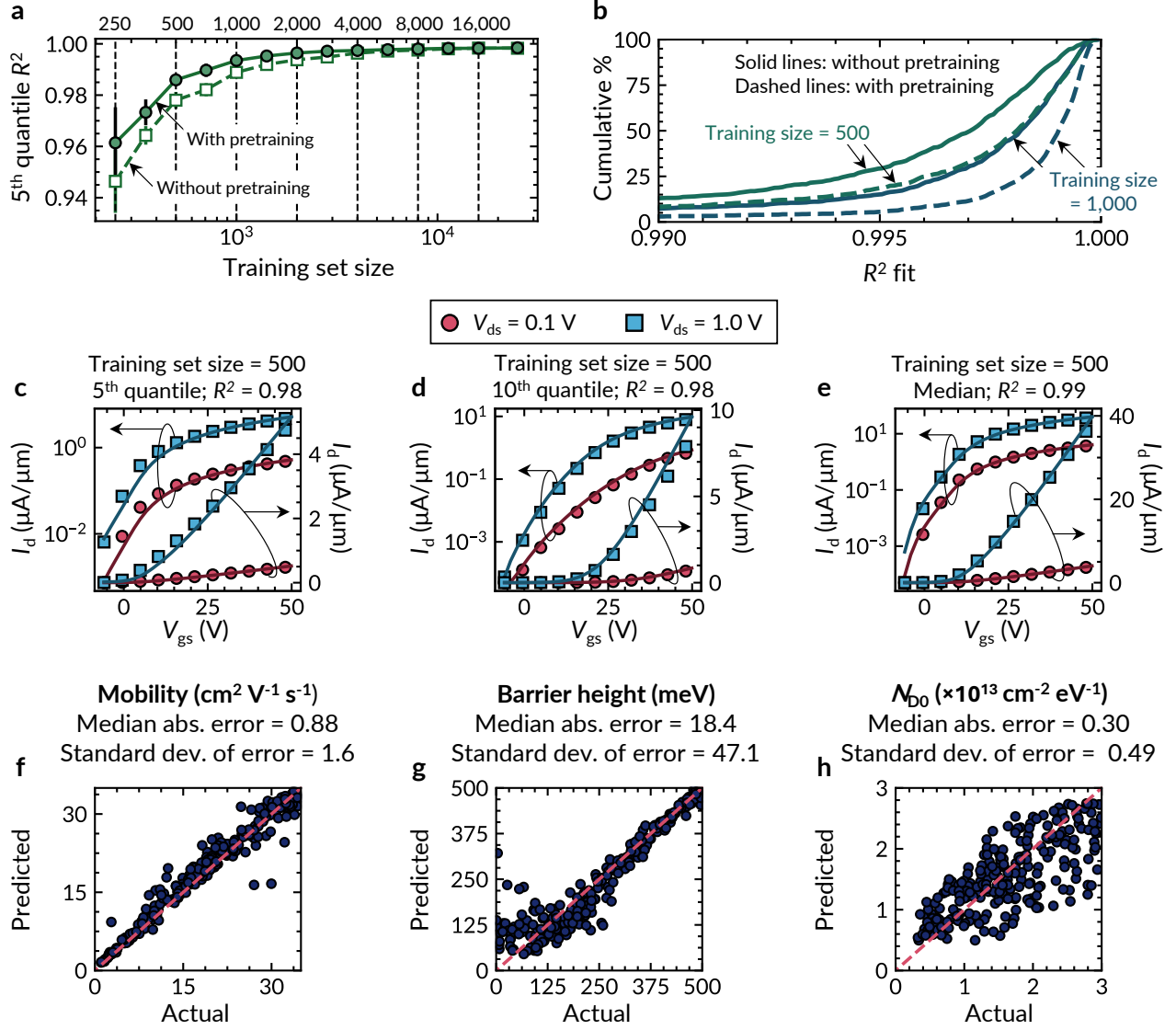


Figure 4: Performance of the inverse network on the simulated test set (a) The 5th quantile (i.e., worst 5%) R^2 attained by the inverse neural network as a function of training size, with and without pre-training, and (b) sample cumulative R^2 fits achieved by the inverse neural network, with (solid lines) and without (dashed lines) pre-training. Error bars in (a) show standard deviations across five bootstrapped runs; error bars are often small and are not always visible. Sample current vs. gate-to-source voltage fits after training the inverse neural network on 500 devices, showing the reverse-engineered fits corresponding to (c) the 5th quantile, (d) 10th quantile, and (e) median R^2 (symbols: original physics-based simulations; lines: estimated I_d - V_{gs} curves obtained using reverse-engineered parameters). The data are shown on both logarithmic (left) and linear axes (right), at $V_{ds} = 0.1$ V (red) and 1.0 V (blue). Actual vs. predicted values for (e) mobility, (f) Schottky contact barrier height, and (g) peak donor density. The pink dashed lines are the lines of zero error, i.e., where predicted and actual values match perfectly.

This reduction in training set size makes it feasible to train the neural network to train on data generated by computationally-intensive models: for example, assuming parallelization to 32 cores, it would take ~ 30 minutes to generate a 500 device training set if using a TCAD solver like Sentaurus with \sim two minutes per I_d - V_{gs} curve, or ~ 1.25 days if using a quantum-transport solver (e.g., the non-equilibrium Green's function

method) with \sim one hour per I_d - V_{gs} curve. It would take \sim 1 day or \sim 1 month (respectively) to generate these training sets if using a fitting approach that requires training on 20,000 devices; thus, the approach presented here reduces a day-long generation task to something that can be accomplished in under an hour, or an (often) unfeasibly long task to something that can be accomplished in a day.

Next, we investigate the accuracy of the extracted parameters, plotting the actual *vs.* predicted values for mobility, Schottky contact barrier height, and peak donor density in **Figures 4f-h**. We show similar plots for all model parameters in **Supplementary Section 6**. Here, we find that the mobility and Schottky barrier height can both be extracted with relatively low median absolute errors of $0.88 \text{ cm}^2 \text{ V}^{-1} \text{ s}^{-1}$ and 18.4 meV , respectively, representing 2.6% and 3.7% of their nominal ranges. The standard deviation of the mobility error is also quite small at $1.9 \text{ cm}^2 \text{ V}^{-1} \text{ s}^{-1}$ (5.6% of its nominal range), whereas the standard deviation for the Schottky barrier height (47.1 meV) is 9.4% of its nominal range. However, from **Figure 4g**, most of these errors occur when the actual Schottky barrier height is comparable to the thermal energy $k_B T$ (where k_B is the Boltzmann constant and $T = 300 \text{ K}$ is the absolute temperature), which makes sense physically: once the barrier is “small enough,” small deviations will not meaningfully affect the contact resistance or the resultant I_d .

We find larger errors in the other model parameters – for example, as shown in **Figure 4h**, the median absolute error for the peak donor density N_{D0} ($3.0 \times 10^{12} \text{ cm}^{-2} \text{ eV}^{-1}$) represents 11.1% of its nominal range, and the relatively large standard deviation ($4.9 \times 10^{12} \text{ cm}^{-2} \text{ eV}^{-1}$) represents 18.1% of this range. We speculate that we see larger errors in these parameters because they have some mutual redundancy: for example, if the peak donor density is underestimated, then the overall donor profile could still be closely matched by increasing its standard deviation to compensate. In comparison, the mobility and Schottky contact barrier height both influence the I_d - V_{gs} curves uniquely compared to other parameters. In other words, if these parameters are estimated incorrectly, the overall I_d - V_{gs} curves cannot be matched by adjusting other model parameters to compensate, leading to lower error in their extractions.

Experimental validation: measured I_d - V_{gs} data from monolayer WS₂ transistors

We validate our deep learning approach experimentally by using a test set collected from 52 monolayer WS₂ transistors that were fabricated across 3 separate chips.²⁹ All measured working devices were included, except for one outlier that could not achieve an on-state current of at least $1 \mu\text{A}/\mu\text{m}$ at $V_{gs} = 50 \text{ V}$, leaving a total of 51 devices in the test set. These devices follow the geometry shown in **Figure 2a** with a channel length of 500 nm, 100 nm SiO₂ back-gate insulators, and nickel contacts (see **Supplementary Section 7** for full experimental details). We choose this channel length because it offers an intermediate regime where both the channel and contacts will influence I_d , allowing us to characterize both the channel and contacts. To match our physics-based training sets, we perform I_d - V_{gs} sweeps at $V_{ds} = 0.1$ and 1 V (all curves at $V_{ds} = 1 \text{ V}$ are plotted in **Figure 5a**) and then feed the measured data into our inverse network after training it on physics-based simulations from 500 devices. We then extract the 8 model parameters listed in **Table I** and perform new Sentaurus TCAD simulations using these predicted parameters.

We plot the cumulative R^2 between the TCAD-simulated I_d - V_{gs} curves (simulated using the predicted input parameters) and original experimental data in **Figure 5b**, finding that the 25th quantile (worst 25%), median, and 75th quantile (best 25%) R^2 fits for the test set are 0.984, 0.990, and 0.994, respectively. We plot the

corresponding I_d - V_{gs} fits in **Figures 5c-e**, along with fits for all 51 devices in the experimental test set in **Supplementary Section 7**. The I_d - V_{gs} curves are plotted on both logarithmic and linear axes, as is customary for displaying electrical transistor data.

A key advantage of this deep learning approach is that once the neural networks are trained, we can rapidly characterize many devices simultaneously to study variation across one or more chips. For example, we plot the cumulative histogram of the maximum measured current at $V_{gs} = 50$ V and $V_{ds} = 1$ V, $I_d^{(max)}$, in **Figure 5f**, as well as the extracted electron mobility and Schottky contact barrier heights in **Figures 5g,h**. We find that the extracted mobility and barrier heights show significant variation, agreeing well (qualitatively) with the experimental variation in **Figures 5a,f**. Overall, we anticipate that this approach could be used to facilitate characterization and analysis of large distributions of devices, so long as the ranges of variables in the training set are sufficiently broad to encapsulate the variation of these relevant parameters experimentally.

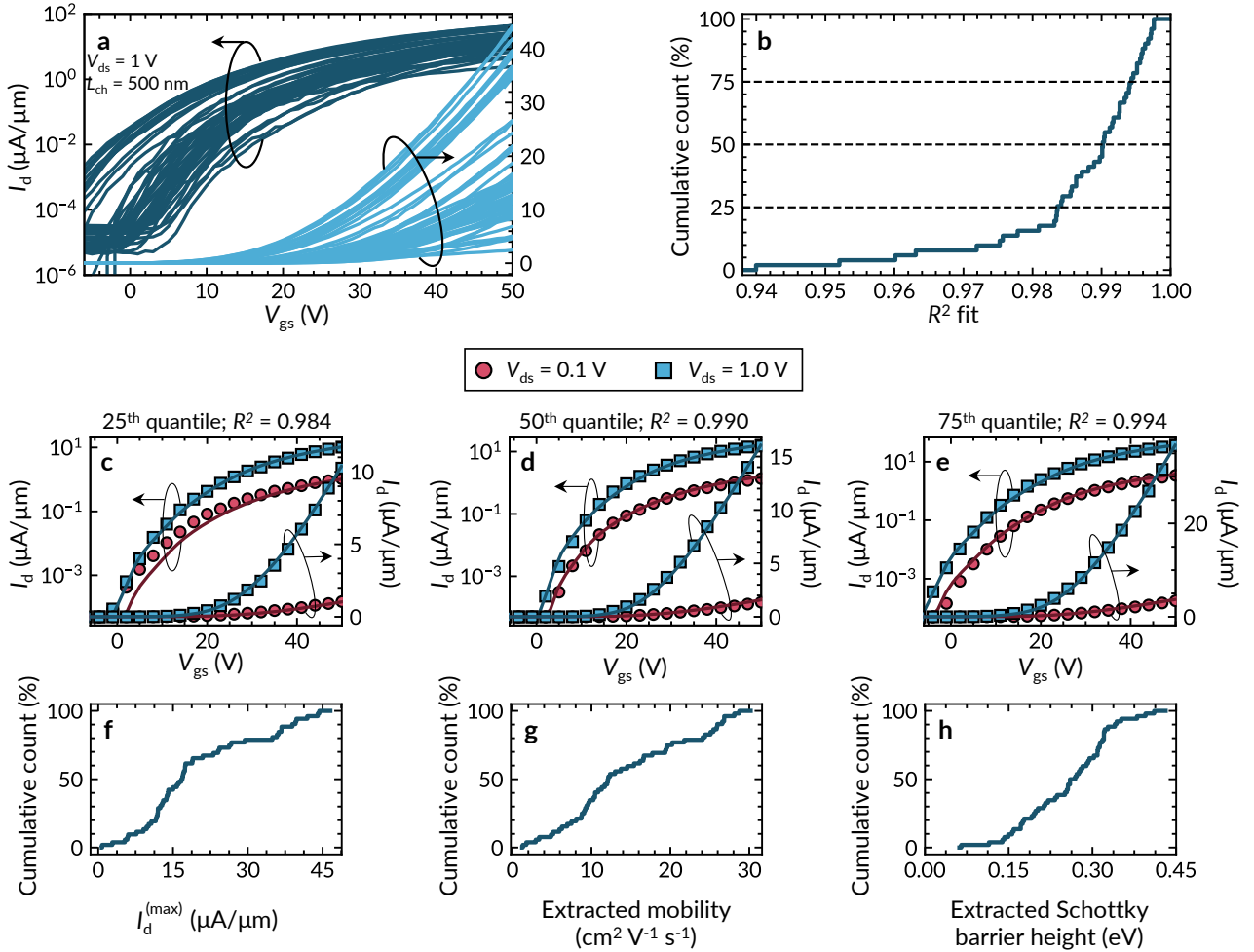


Figure 5: Performance of the inverse network on experimentally measured test devices. (a) All 51 measured I_d - V_{gs} curves for monolayer WS_2 transistors ($V_{ds} = 1$ V) in our experimental test set, shown both on logarithmic (left) and linear (right) y-axes. (b) Cumulative histogram showing the R^2 fits between the original experimental data and devices reverse-engineered by an inverse neural network trained on 500 sets of physics-based simulations. Sample I_d - V_{gs} fits for (c) the 25th quantile, (d) median, and (e) 75th quantile R^2 , showing good agreement between the experimental data (symbols) and our reverse-engineered fits (lines). Data are shown on both logarithmic (left) and linear axes (right), at $V_{ds} = 0.1$ V (red) and 1.0 V (blue). Cumulative histograms for (f) the experimental $I_d^{(max)}$, (g) the extracted mobility, and (h) the extracted Schottky barrier height.

Figures 5g,h also addresses questions about the distribution of electron mobility and contact resistance one can expect for a particular WS₂ synthesis and fabrication approach. For example, the mobility includes information about the electron effective mass and scattering mechanisms with lattice vibrations and defects, both in the WS₂ film and its substrate. In other words, **Figure 5g** could be used to obtain information about the defect distribution in such WS₂ films. Similarly, **Figure 5h** can be used to understand how the deposition of the metal (nickel) affects the transistor contacts. We caution that the distributions shown here are for unoptimized academic devices. One must increase the mobility, decrease the Schottky barrier height, and tighten these distributions before these transistors can become competitive in the semiconductor industry.

Model generalization and fitting many physical parameters simultaneously

Until now, we have confined our discussion to 2D semiconductor transistors simulated by TCAD using 8 fitting parameters. However, model fitting is routinely applied to other types of devices, often using highly dimensionalized models with many parameters.^{11,12} In **Supplementary Section 8**, we study how our approach scales with the complexity of the I_d - V_{gs} model by applying the same methodology to train a neural network to predict the input parameters of GaN high-electron-mobility transistors (HEMTs) simulated with the industry-standard ASM-HEMT compact model.¹¹ We find that training becomes more difficult when fitting more physical transistor parameters simultaneously; this result is an expected consequence of the *curse of dimensionality*³⁰ encountered when fitting high-dimensional data, as the size of the parameter space grows exponentially as additional parameters are added (e.g., a space with N dimensions sampled along k values has size k^N). Nevertheless, we demonstrate that we can still achieve good fits when fitting 15 or 25 or 35 parameters with a training set containing data from \sim 1,000 or 4,000 or 16,000 unique devices, respectively.

These scaling trends indicate that the method proposed in this work could be applied to fit transistor data even to complicated models with many unknown parameters, as long as generating the appropriately sized training set remains computationally tractable. This consideration varies tremendously from model to model: for example, generating such large training sets could be trivial for compact models implemented in Verilog-A, including the ASM-HEMT model¹¹ considered above, which can be used to generate thousands of I_d - V_{gs} curves per second. It may be significantly harder to generate such large data sets with rigorous physics-based models, especially in the face of hardware limitations and/or limited licenses, which may restrict parallelizability. However, we also highlight that once a neural network is fully trained, it can be used repeatedly to fit many devices with minimal computation cost, e.g., as we do with experimental monolayer WS₂ devices in **Figure 5**. Thus, the up-front cost of acquiring larger training sizes may remain acceptable if a fitting procedure must be repeated multiple times, especially when considering the cost of human expert time.

Conclusions

In conclusion, we have developed a deep learning approach to automate parameter extraction (TCAD fitting) for transistors based on their current *vs.* gate-to-source voltage characteristics. We significantly reduce the number of devices required in our training set compared to those demonstrated in prior works, and we demonstrate excellent fits on experimental 2D transistors using models trained on physics-based simulations from 500 devices. This approach also generalizes well to other types of transistors and models (e.g., GaN high-electron-mobility transistors with up to 35 unknown parameters in the ASM-HEMT model), as long as

acquiring larger training sets remains computationally feasible. Thus, we anticipate that the results of this study will facilitate fitting experimental device measurements to both physics-based and compact models alike.

In this work, we have not investigated how noisy or partially corrupted measurements affect the accuracy of this method. Further, a disadvantage of our machine learning approach (and similar approaches put forward in previous works⁵⁻¹⁰) is that fitting devices with different geometries (e.g., varying channel length or oxide thickness, or changing the gating configuration between bottom-, top-, or dual-gated devices) require that training sets be regenerated and neural networks be retrained. Addressing these issues would expand the robustness of the method implemented here and remain research directions for future work. To facilitate such work, we have uploaded our data sets and Python code to an online GitHub repository.¹⁹

Author Contributions

R.K.A.B. conceived the project idea. R.K.A.B. and Y.S. configured the Sentaurus TCAD model. R.K.A.B., J.U., H.F.G., developed and verified the machine learning models. L.H., T.P., Z.Z., and K.N. fabricated monolayer semiconductor devices. L.H., T.P., and K.N. performed electrical measurements. R.K.A.B., H.G., A.K., A.J.M., and E.P. analyzed and interpreted the results. E.P. and A.J.M. supervised the research. R.K.A.B. and E.P. wrote the manuscript with input from all authors. All authors read and approved the final version of the manuscript.

Data Availability Statement

Sample training and test data used in this study is available in an online GitHub repository.¹⁹ All other data that support the findings of this study are available from the corresponding author upon request.

Code Availability Statement

Code that supports the findings of this study is available in an online GitHub repository.¹⁹

Conflicts of Interest

The authors declare no conflicts of interest.

Acknowledgements

R.K.A.B. acknowledges support from the Stanford Graduate Fellowship (SGF) and NSERC PGS-D programs. J.U. acknowledges support from the US Department of Energy, Office of Science, Basic Energy Sciences, Materials Sciences and Engineering Division, under contract DE-AC02-76SF00515. H.F.G. acknowledges support from the Stanford Electrical Engineering Research Experience for Undergraduates (REU) program, the Stanford Undergraduate Research and Independent Projects Program in the form of a Small Grant, and the SUPREME Undergraduate Microelectronics Fellowship program. K.N. acknowledges support from the Stanford Graduate Fellowship (SGF) and the National Science Foundation Graduate Research Fellowship Program (NSF-GRFP). The authors also acknowledge partial support from the Stanford SystemX Alliance and from SUPREME, one of seven centers in JUMP 2.0, a Semiconductor Research Corporation (SRC) program sponsored by DARPA.

References

- 1 Huang, X., Liu, C. & Zhou, P. 2D semiconductors for specific electronic applications: from device to system. *npj 2D Materials and Applications* **6**, 51, doi:10.1038/s41699-022-00327-3 (2022).
- 2 Lu, B. *et al.* Amorphous oxide semiconductors: From fundamental properties to practical applications. *Current Opinion in Solid State and Materials Science* **27**, 101092, doi:https://doi.org/10.1016/j.cossms.2023.101092 (2023).
- 3 Franklin, A. D., Hersam, M. C. & Wong, H. S. P. Carbon nanotube transistors: Making electronics from molecules. *Science* **378**, 726-732, doi:10.1126/science.abp8278 (2022).
- 4 Martinez, R. P. *et al.* Compact Model Parameter Extraction via Derivative-Free Optimization. *IEEE Access* **12**, 123224-123235, doi:10.1109/ACCESS.2024.3453198 (2024).
- 5 Chen, J.-H., Chavez, F., Tung, C.-T., Khandelwal, S. & Hu, C. A single neural network global I-V and C-V parameter extractor for BSIM-CMG compact model. *Solid-State Electronics* **216**, 108898, doi:https://doi.org/10.1016/j.sse.2024.108898 (2024).
- 6 Singhal, A., Pahwa, G. & Agarwal, H. A Novel Physics Aware ANN-Based Framework for BSIM-CMG Model Parameter Extraction. *IEEE Transactions on Electron Devices* **71**, 3307-3314, doi:10.1109/TED.2024.3381917 (2024).
- 7 Ashai, A. *et al.* Deep Learning-Based Fast BSIM-CMG Parameter Extraction for General Input Dataset. *IEEE Transactions on Electron Devices* **70**, 3437-3441, doi:10.1109/TED.2023.3278615 (2023).
- 8 Chavez, F., Davis, D. T., Miller, N. C. & Khandelwal, S. Deep Learning-Based ASM-HEMT I-V Parameter Extraction. *IEEE Electron Device Letters* **43**, 1633-1636, doi:10.1109/LED.2022.3197800 (2022).
- 9 Kao, M. Y., Chavez, F., Khandelwal, S. & Hu, C. Deep Learning-Based BSIM-CMG Parameter Extraction for 10-nm FinFET. *IEEE Transactions on Electron Devices* **69**, 4765-4768, doi:10.1109/TED.2022.3181536 (2022).
- 10 Chen, J.-H., Chavez, F., Tung, C.-T., Khandelwal, S. & Hu, C. A multi-stage neural network I-V and C-V BSIM-CMG model global parameter extractor for advanced GAAFET technologies. *Solid-State Electronics* **226**, 109081, doi:https://doi.org/10.1016/j.sse.2025.109081 (2025).
- 11 Dasgupta, A., Ghosh, S., Chauhan, Y. S. & Khandelwal, S. in *2015 IEEE International Conference on Electron Devices and Solid-State Circuits (EDSSC)*. 495-498 (2015).
- 12 Dunga, M. V., Lin, C.-H., Niknejad, A. M. & Hu, C. in *FinFETs and Other Multi-Gate Transistors* (ed Jean-Pierre Colinge) 113-153 (Springer US, 2008).
- 13 Smidstrup, S. *et al.* QuantumATK: an integrated platform of electronic and atomic-scale modelling tools. *Journal of Physics: Condensed Matter* **32**, 015901, doi:10.1088/1361-648X/ab4007 (2020).
- 14 Datta, S. Nanoscale device modeling: the Green's function method. *Superlattices and Microstructures* **28**, 253-278, doi:https://doi.org/10.1006/spmi.2000.0920 (2000).
- 15 Camsari, K. Y., Chowdhury, S. & Datta, S. in *Springer Handbook of Semiconductor Devices* (eds Massimo Rudan, Rossella Brunetti, & Susanna Reggiani) 1583-1599 (Springer International Publishing, 2023).
- 16 Jeong, C. *et al.* Bridging TCAD and AI: Its Application to Semiconductor Design. *IEEE Transactions on Electron Devices* **68**, 5364-5371, doi:10.1109/TED.2021.3093844 (2021).
- 17 Lee, Y., Cao, J. & Luisier, M. Atomistic Simulation of Nanoscale Devices. *IEEE Nanotechnology Magazine* **17**, 4-14, doi:10.1109/MNANO.2023.3278968 (2023).
- 18 Martín, A. *et al.* TensorFlow: Large-Scale Machine Learning on Heterogeneous Systems. (2015).
- 19 Bennett, R. K. A. Deep learning for transistor parameter extraction (GitHub repository). Available online: <https://github.com/RKABennett/deep-learning-for-transistor-parameter-extraction>.
- 20 Djomehri, I. J. & Antoniadis, D. A. Inverse modeling of sub-100 nm MOSFETs using I-V and C-V. *IEEE Transactions on Electron Devices* **49**, 568-575, doi:10.1109/16.992864 (2002).
- 21 Synopsys, Inc. Sentaurus Device Manual. (2017).
- 22 Liu, D., Tan, Y., Khoram, E. & Yu, Z. Training Deep Neural Networks for the Inverse Design of Nanophotonic Structures. *ACS Photonics* **5**, 1365-1369, doi:10.1021/acsp Photonics.7b01377 (2018).

- 23 Jenkins, T. M., Nelson, W. R. & Rindi, A. *Monte Carlo transport of electrons and photons*. Vol. 38 (Springer Science & Business Media, 2012).
- 24 De La Cruz Blas, C. A., Gómez-Polo, C., Carlosena, A. & Olivera, J. A phenomenological spice model for magneto-impedance sensors. *International Journal of Circuit Theory and Applications* **40**, 275-286, doi:<https://doi.org/10.1002/cta.723> (2012).
- 25 Woo, S. *et al.* Machine-Learning-Based Compact Modeling for Sub-3-nm-Node Emerging Transistors. *Electronics* **11**, 2761 (2022).
- 26 Vladimirescu, A. *The Spice Book*. (John Wiley & Sons, Inc., 1994).
- 27 Gupta, A., Karahan, E. A., Bhat, C., Sengupta, K. & Khankhoje, U. K. Tandem Neural Network Based Design of Multiband Antennas. *IEEE Transactions on Antennas and Propagation* **71**, 6308-6317, doi:[10.1109/TAP.2023.3276524](https://doi.org/10.1109/TAP.2023.3276524) (2023).
- 28 Sullivan, J., Mirhashemi, A. & Lee, J. Deep learning-based inverse design of microstructured materials for optical optimization and thermal radiation control. *Scientific Reports* **13**, 7382, doi:[10.1038/s41598-023-34332-3](https://doi.org/10.1038/s41598-023-34332-3) (2023).
- 29 Zhang, Z. *et al.* Chemically Tailored Growth of 2D Semiconductors via Hybrid Metal–Organic Chemical Vapor Deposition. *ACS Nano* **18**, 25414-25424, doi:[10.1021/acsnano.4c02164](https://doi.org/10.1021/acsnano.4c02164) (2024).
- 30 Köppen, M. in *5th online world conference on soft computing in industrial applications (WSC5)*. 4-8 (2000).

Supplementary Information

Deep Learning to Automate Parameter Extraction and Model Fitting of Two-Dimensional Transistors

Robert K. A. Bennett,¹ Jan-Lucas Uslu,^{2,3} Harmon Gault,¹ Asir Intisar Khan,¹ Lauren Hoang,¹ Tara Peña,¹ Kathryn Neilson,¹ Young Suh Song,¹ Zhepeng Zhang,^{3,4} Andrew J. Mannix,^{3,4} Eric Pop^{1,3,4,5,*}

¹Department of Electrical Engineering, Stanford University, Stanford, CA 94305, USA

²Department of Physics, Stanford University, Stanford, CA 94305, USA

³Stanford Institute for Materials and Energy Sciences, SLAC National Accelerator Laboratory, Menlo Park, CA 94025, USA

⁴Department of Materials Science and Engineering, Stanford University, Stanford, CA 94305, USA

⁵Department of Applied Physics, Stanford University, Stanford, CA 94305, USA

*Contact: epop@stanford.edu

Supplementary Section 1: Details for Sentaurus simulations of two-dimensional transistors

We use Sentaurus Device,¹ an industry-standard technology computer-aided design (TCAD) simulator, for the physics-based simulations used in this work. We perform simulations in a two-dimensional domain using the cross-section shown in **Figure 2a** from the main text, where the width dimension of the device (into the page, perpendicular to the channel) is treated as periodic. Here, the default drift-diffusion model for transport is solved self-consistently with electrostatics, which are captured by Poisson's equation.

We treat the 2D semiconductor/metal contacts as Schottky contacts using Sentaurus Device's Schottky barrier model, and we enable tunneling through the barrier using Sentaurus Device's Schrodinger model on a nonlocal mesh. Although Fermi level pinning is known to affect the barrier height of 2D semiconductor/metal contacts,² Sentaurus Device does not presently have an established model for this pinning. To achieve a specific nominal barrier height, we therefore use the 2D semiconductor's electron affinity as a free parameter, with the resultant barrier height given by $\phi_{B0} = \chi_s - \phi_m$, where χ_s is the 2D semiconductor's electron affinity and $\phi_m = 5.01$ eV is the work function of nickel. Gate-voltage-dependent contact resistance, an important experimental consideration,³ is incorporated in our Sentaurus Device simulations automatically, as the electric field from the back-gate electrode electrostatically influences the 2D semiconductor underneath the metal.

We assign the monolayer 2D semiconductor an electronic band gap of 2.2 eV (larger than the optical band gap dictated by the exciton binding energy),^{4,5} a channel thickness of 0.62 nm,⁶ and in-plane and out-of-plane relative permittivities of 14 and 7,⁷ respectively. We approximate the density of states using Sentaurus Device's effective mass model (as implemented by setting Formula=2).¹ We treat donor-like states (often attributed to chalcogen defects in a 2D semiconductor like MoS₂ or WSe₂) as states located at the 2D semiconductor/oxide interface, and we assume band-tail acceptor-like states are uniformly distributed across the 2D channel thickness.

Supplementary Section 2: Descriptions of model parameters for two-dimensional transistors

In **Table 1** of the main text, we list our fitting parameters alongside their lower and upper bounds. Here, we briefly explain the physical significance of each parameter and justify these bounds.

Mobility: A semiconductor’s electron mobility is the proportionality constant between the electron speed and the applied electric field, assuming drift-diffusion transport (which is valid for the relatively long 500 nm channel lengths considered in this work). Typical academic 2D transistors often yield a mobility of the order $\sim 10 \text{ cm}^2 \text{ V}^{-1} \text{ s}^{-1}$; here, we use a range of 1 to $35 \text{ cm}^2 \text{ V}^{-1} \text{ s}^{-1}$ to encapsulate this typical value. We note that electron mobilities above $35 \text{ cm}^2 \text{ V}^{-1} \text{ s}^{-1}$ are certainly possible in optimized devices with fewer defects; to fit such devices, the training set should be expanded to incorporate these higher mobilities.

Schottky barrier height: The Schottky barrier height is the energy barrier which a carrier must overcome to be injected from the metal contact to the semiconductor channel or vice versa. The Schottky barrier height is a function of its electrostatic environment and is hence not an intrinsic material or device parameter.⁸ When we report Schottky barrier heights in this work, we specifically refer to the *nominal* Schottky barrier height $\phi_{B0} = \chi_s - \phi_m$, where χ_s is the semiconductor’s electron affinity and ϕ_m is the metal contact’s work function.

Contacts between 2D semiconductors and conventional metals are affected by Fermi level pinning, whereby metal-induced and/or defect-induced gap states cause the Fermi energy to become pinned at the charge neutrality level.² As a result, even though the work functions of metals and the electron affinities of two-dimensional semiconductors are well known, the real barrier height is not simply $\chi_s - \phi_m$. Processing conditions, the number of defects in the 2D semiconductor, strain profiles, and other non-idealities make accurately predicting this value difficult. Our previous experimental estimates for nickel + monolayer WS_2 systems put the barrier height between 170 and 400 meV;⁹ here, we expand this range to 10 to 510 meV.

Density of states: a semiconductor’s effective density of states N_C refers to the number of energy levels in which electrons can reside, with a larger density of states meaning that more electrons can become available to conduct current (i.e., a higher density of states means higher conductance, assuming the same mobility). The density of states can be estimated from simulation techniques, such as density functional theory; however, local strain profiles, spacing of higher-energy valleys, and other extrinsic factors can affect a material’s effective density of states. Typically, $N_C \approx 5 \times 10^{11} \text{ cm}^{-2}$ for 2D semiconductors;¹⁰ here, because of these uncertainties, we use a large expanded range of 2×10^{11} to $9 \times 10^{12} \text{ cm}^{-2}$ to comfortably encapsulate the expected N_C .

Donor defect profiles: experimental studies suggest that sulfur vacancies in two-dimensional semiconductors may act as electron donors.¹¹ Photoluminescence studies suggest that these vacancies follow Gaussian distributions with respect to energy, with shallow defects located a few tenths of an eV below the conduction band edge and deep states located nearer to the mid gap. Since we do not probe the deep subthreshold region in this work, we consider only the shallow defect states. A previous work¹¹ assigns these states a median energy $E_{D,\text{mid}} \approx 0.15 \text{ eV}$ below the conduction band edge and an energy width (i.e., standard deviation) $\sigma_D \approx 72 \text{ meV}$ (from Figure 3c of ref. ¹¹). See **Figure 2b** in the main text for a visual depiction of this profile and these parameters. Here, we use these as rough center points for our estimated ranges, sampling $E_{D,\text{mid}}$, and σ_D both between 20 – 200 meV. The peak concentration N_{D0} for these donor states can vary tremendously depending

on film quality, making it difficult to estimate based on previous works. Here, we intentionally use a large range of $3 \times 10^{12} - 3 \times 10^{13} \text{ eV}^{-1} \text{ cm}^{-2}$ to encapsulate reasonable values for N_{D0} .

Band tail acceptor-like defect profiles: experimentally, 2D semiconductors do not have sharp conduction band edges; instead, the density of states decreases exponentially as E decreases below E_C . Although some works have investigated the influence of these band tail states on transport, the precise implications of band tails on electron transport in 2D semiconductors are unclear. In particular, the mobility of electrons contributed by band tail states is unclear, although it appears to be much less than that of conduction band electrons.

In this work, we adapt a convention previously applied for amorphous oxide semiconductors and model band tails as acceptor states and assign them 0 mobility.¹² This assumption is also made in the multiple-trap-and-release model, which is frequently used to describe transport in organic semiconductors.¹³ Even though these states do not participate directly in conduction, their electrostatics are still considered explicitly: a higher density of tail states shifts the threshold voltage to the right and worsens subthreshold swing.

Previous work has estimated that the peak band tail density N_{A0} and characteristic energy decay length σ_A that characterize the exponential distribution [Eq. (5) in the main text] vary from $3 \times 10^{12} - 1.8 \times 10^{13} \text{ eV}^{-1} \text{ cm}^{-2}$ and from $\sim 56 \text{ meV}$ to 170 meV for similar 2D semiconductor systems.¹⁴ Here, we expand these ranges to $6 \times 10^{11} - 3.7 \times 10^{13} \text{ eV}^{-1} \text{ cm}^{-2}$ and $50 - 300 \text{ meV}$, respectively, to comfortably encapsulate these initial estimates.

Supplementary Section 3: Feature engineering and ablation study

The inverse neural network shown in **Figure 3a** of the main text aims to reverse-engineer physics-based simulation model parameters from electrical measurements. For each device, we input drain current *vs.* gate-to-source voltage (I_d - V_{gs}) curves at 32 fixed V_{gs} values, with applied drain-to-source biases $V_{ds} = 0.1$ and 1 V. For each V_{ds} , we also perform simple feature engineering by inputting each current in logarithmic space, along with $\partial I_d/\partial V_{gs}$ and $\partial \log_{10} I_d/\partial V_{gs}$, for a total of eight unique features per device.

In principle, model parameters can be fit from experimental or simulated data using I_d - V_{gs} data at a single V_{ds} . Further, because derivatives and logarithms are implicitly contained within the data itself, seven of our eight features may seem unnecessary. Here, we justify from domain knowledge why one should expect that including these features should improve the performance of the neural network. After, we demonstrate empirically with an ablation study that failing to include these terms results in worse performance.

Including multiple drain biases: transistors with Schottky contacts, such as experimentally relevant two-dimensional transistors, can be conceptually thought of as an ideal ohmic transistor in series with two separate diodes that represent the source and drain.¹⁵ These diodes are nonlinear circuit elements, meaning here that their resistances are functions of the voltage drops across them. Including multiple drain biases should help to ensure that the resistance of both the channel and the source/drain take on additional unique profiles, and thus aid in estimating the Schottky barrier height, one of our key fitting parameters.

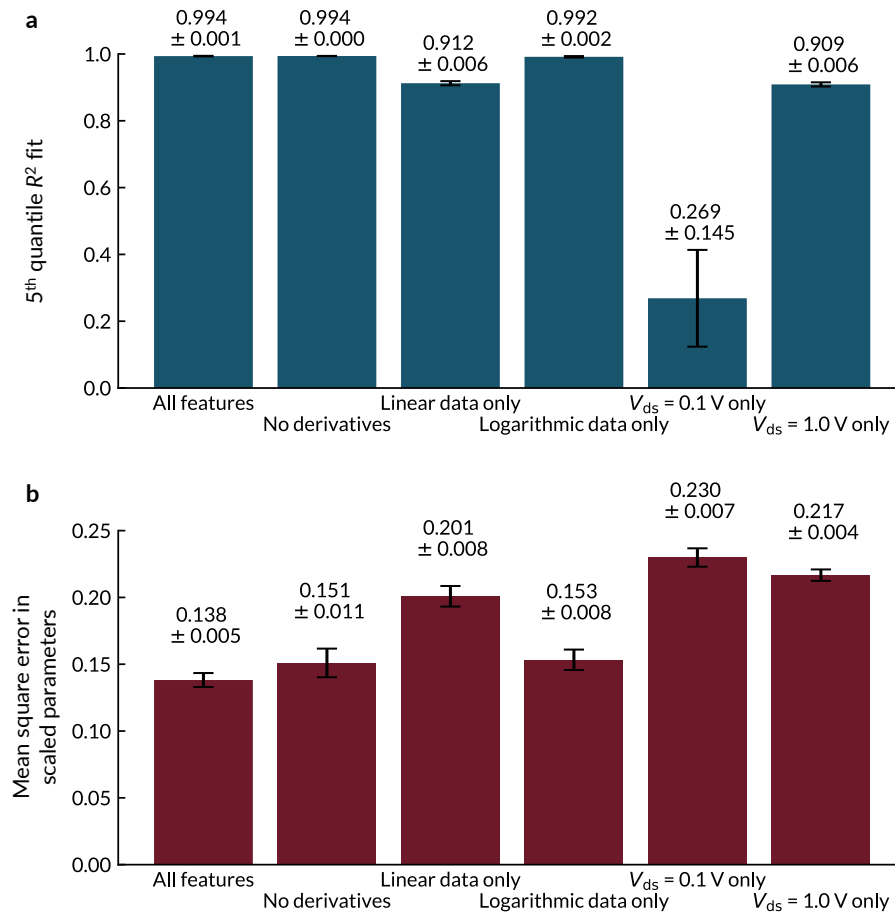
Including logarithmic I_d - V_{gs} data: The off-state of the transistor provides essential information about key physical model parameters, including the acceptor and donor profiles that we parameterize using the five separate fitting parameters in **Table I** in the main text. However, I_d in the off-state (low V_{gs}) can be orders of magnitude smaller than I_d in the on-state. For example, in **Figure 5a** in the main text, the ratio of on- to off-state current for many of our experimental WS₂ transistors is $>10^5$. If we did not take the logarithm of I_d , differences in off-state currents would be washed out, causing us to lose essential information in the data.

Including derivatives: mobility is commonly extracted from transistor measurements by finding the transconductance $g_m = \partial I_d/\partial V_{gs}$ and then estimating the mobility as $\mu = g_m/(C_g V_{gs} - V_T)$, where C_g is the gate capacitance. This mobility extraction is frequently made non-trivial by *contact gating*, i.e., the gate voltage modulates R_C , causing g_m to change from extrinsic factors, such as the Schottky barrier height.^{3,16} Similarly, the subthreshold swing (inversely proportional to $\partial \log_{10} I_d/\partial V_{gs}$ in the off-state) can often be correlated to defect profiles [acceptor and donor, e.g., **Eqs.(3) and (4)** in the main text]. Thus, we explicitly input the derivatives to make these parameters easier for the neural network to extract.

Ablation study: we empirically verify the importance of including each feature by ablating them from the input matrix, (i.e., by setting all entries in the relevant feature columns to 0), and then re-training the neural networks as before. This process allows us to examine how withholding the feature impacts the performance of the final trained network. For each ablation, we use 1,000 devices in our training and development sets combined and perform 5 different runs, using the same 5 sets of training and development data for each ablation. Afterwards, we test the performance of the neural network by reverse-engineering the fitting parameters, estimating the corresponding I_d - V_{gs} curves for these extracted parameters, and then calculating the

R^2 fit between the original and estimated I_d - V_{gs} data. Here, all tests consider I_d - V_{gs} curves at $V_{ds} = 0.1$ and 1 V, where the R^2 fit is averaged in both linear and logarithmic space at both V_{ds} values (same as in the main text).

As shown in **Supplementary Figure S1a**, we find that the resultant I_d - V_{gs} fits become quite poor when we fail to include the logarithmic data or when we remove either drain bias. We find that the quality of the I_d - V_{gs} fits remain acceptable when we do not include the derivatives of the I_d - V_{gs} curves and when we include only the logarithmic data; however, as shown in **Supplementary Figure S1b**, the error in the fitting parameter increases if we exclude these features.



Supplementary Figure S1: Impact of ablating features on model performance. (a) The 5th quantile (i.e., worst 5%) R^2 fit (higher is better) and (b) mean square error in scaled parameters (lower is better) for different configurations of input features. We find that when removing our engineered features, the resultant fits become worse and the error in the fitting parameters increases. “Linear data only” and “logarithmic data only” denote that only the linear-scale I_d - V_{gs} curves and their derivatives, or logarithmic-scale I_d - V_{gs} curves and their derivatives, respectively, were included in the input matrix.

Supplementary Section 4: Details for pre-processing, training, bootstrapping, and testing

Interpolation

Our forward neural network (**Supplementary Figure S2a**) outputs I_d - V_{gs} curves along 32 fixed V_{gs} values, evenly spaced from -6 to 50 V. (Our Sentaurus Device simulations stopped just outside of the V_{gs} range of -6 to 50 V; hence, we actually use a range of -5.9 to 49.9 V throughout this work.) Our inverse neural network (**Figure 3a** in the main text) accepts I_d - V_{gs} curves and their derivatives along the same V_{gs} points. In our Sentaurus Simulations, we compute drain current *vs.* gate-to-source voltage (I_d - V_{gs}) profiles across a similar range of V_{gs} values; however, the exact V_{gs} grid changes between simulations to maximize computational efficiency and hence does not align perfectly with the 32 fixed V_{gs} values in the network's output and input layers. Therefore, we pre-process our simulated I_d - V_{gs} data by interpolating I_d along the fixed V_{gs} points required by our neural networks, using linear and logarithmic interpolation to interpolate I_d and $\log_{10}I_d$, respectively. This interpolation scheme and all pre-processing steps are implemented in `process_devices.py` in our GitHub Repository.¹⁷

Noise floor

Experimentally, the lowest drain current that can be reliably measured is limited by the *noise floor* of the measurement instrument. For our experimental monolayer WS₂ transistor measurements, our noise floor is $\sim 10^{-5}$ $\mu\text{A}/\mu\text{m}$ (**Figure 5a** in the main text). Our Sentaurus Device simulations allow us to simulate I_d much less than 10^{-5} $\mu\text{A}/\mu\text{m}$; however, we do not wish to train our neural networks to rely upon features that we do not measure experimentally. Thus, we manually impose a noise floor of 5×10^{-5} $\mu\text{A}/\mu\text{m}$ on all Sentaurus-simulated data; that is, any $I_d < 5 \times 10^{-5}$ $\mu\text{A}/\mu\text{m}$ is manually mapped to 5×10^{-5} $\mu\text{A}/\mu\text{m}$. To ensure that the noise floor in our in simulated training/test sets and experimental test sets are identical, we perform the same mapping on our experimental I_d - V_{gs} curves prior to feeding them into our inverse neural network for inference.

Data formatting and min-max scaling

The inverse neural network accepts an input matrix for each device consisting of I_d - V_{gs} and $\log_{10}(I_d)$ - V_{gs} curves and their derivatives (see input in **Figure 3a**), where columns correspond to individual features [e.g., I_d , $\log_{10}(I_d)$, $\partial I_d/\partial V_{gs}$] and rows correspond to the 32 fixed V_{gs} points. For training, these matrices for multiple devices are combined into a third order tensor \mathbf{U} . The first dimension of \mathbf{U} corresponds to the device index, the second dimension corresponds to the 32 fixed V_{gs} points, and the third dimension corresponds to an individual feature. Here, we index starting from 0, and a colon (:) denotes selecting every entry along an index. For example, the slice $\mathbf{U}[j, :, 0]$ is the I_d - V_{gs} curve at $V_{ds} = 0.1$ V for the j^{th} device.

We prepare the scaled tensor $\tilde{\mathbf{U}}$ by min-max scaling \mathbf{U} feature-wise between -1 and 1. Each i^{th} matrix slice along the last dimension of \mathbf{U} is scaled independently using the minimum and maximum values across that individual slice. That is, for each i^{th} slice along the third dimension,

$$\tilde{\mathbf{U}}[:, :, i] = 2 \left(\frac{\mathbf{U}[:, :, i] - \min(\mathbf{U}[:, :, i])}{\max(\mathbf{U}[:, :, i]) - \min(\mathbf{U}[:, :, i])} \right) - 1$$

Next, we consider the output of the forward neural network, V , which is also a third-order tensor. V is a subset of U [U contains I_d - V_{gs} and $\log_{10}(I_d)$ - V_{gs} curves and their derivatives at two drain biases; V contains the I_d - V_{gs} and $\log_{10}(I_d)$ - V_{gs} curves, but not their derivatives]. Thus, V and its scaled equivalent \tilde{V} are built simply by taking the required slices from U and \tilde{U} .

For the i^{th} device, the input of the forward neural network and output of the inverse neural network is the vector $\mathbf{y}^{(i)}$. For training, these vectors are stacked into the matrix \mathbf{Y} , where the first dimension (rows) corresponds to the device index, and the second dimension (columns) corresponds to the fitting parameter. For example, $\mathbf{Y}[i,j]$ corresponds to the j^{th} fitting parameter of the i^{th} device.

We min-max scale \mathbf{Y} between -1 and 1 for each fitting parameter:

$$\tilde{\mathbf{Y}}[:,j] = 2 \left(\frac{\mathbf{Y}[:,j] - \min(\mathbf{Y}[:,j])}{\max(\mathbf{Y}[:,j]) - \min(\mathbf{Y}[:,j])} \right) - 1$$

All min-max scaling is implemented in `process_devices.py` in our GitHub Repository.

Training schemes

We use the Adam Optimizer,¹⁸ as implemented in TensorFlow (Keras),¹⁹ for all training. We train using early stopping, saving only the best performing model, as measured by the validation loss on the development set. During training, we use learning rate annealing. Here, the annealing rate refers to the factor that we multiply the learning rate by at the beginning of each annealing step.

When training the forward neural network, we anneal across 4 steps with an annealing rate of 0.35, using an initial learning rate of 10^{-3} and an early stopping patience of 50. We use a minibatch size of 128 when training the forward network. When pre-training the inverse neural network, we anneal across two steps, each with no more than 50 epochs, using an initial learning rate of 2.5×10^{-4} , an annealing rate of 0.6, and an early stopping patience of 5. After pretraining, we fine-tune the inverse neural network on the original training set used to train the forward network. In this stage, we anneal the inverse neural network across 3 steps with an annealing rate of 0.9. We use an initial learning rate of 2×10^{-5} and an early stopping patience of 40. When we train the inverse neural network without pretraining, as in **Figures 4a,b** in the main text, we use an initial learning rate of 10^{-3} , an annealing rate of 0.8, 10 annealing steps, and a patience of 40 for early stopping. We always use a minibatch size of 256 when training the inverse network.

The pretraining data set uses 100,000 devices when training the inverse neural network to fit data from two-dimensional transistors in (e.g., **Figures 4 and 5** in the main text). When training to fit data from HEMTs in **Supplementary Section 8**, the size of the pretraining data set is the smaller of (i) $100 \times$ the number of compact model simulations or (ii) 1,000,000.

Calculating the current mismatch in the inverse neural network loss function

In Eq. (7) the main text, we introduce the term $E_{I_d}^{(i)}$ to allow the loss function to penalize errors in the predicted I_d - V_{gs} curves for the i^{th} device. Here, $E_{I_d}^{(i)}$ is the sum of three terms that individually quantify errors in the I_d - V_{gs} curves, their slopes, and their curvatures:

$$E_{I_d}^{(i)} = L_{I_d}^{(i)} + L_{\Delta I_d}^{(i)} + L_{\Delta^2 I_d}^{(i)} \quad (\text{S1})$$

where:

$$L_{I_d}^{(i)} = \frac{1}{2N_{V_{ds}}N_{V_{gs}}} \sum_j^{N_{V_{ds}}} \sum_k^{N_{V_{gs}}} \left((I_{\text{true}}^{(i,j,k)} - I_{\text{pred}}^{(i,j,k)})^2 + (\log_{10} I_{\text{true}}^{(i,j,k)} - \log_{10} I_{\text{pred}}^{(i,j,k)})^2 \right) \quad (\text{S2})$$

$$L_{\Delta I_d}^{(i)} = \frac{1}{2N_{V_{ds}}(N_{V_{gs}}-1)} \sum_j^{N_{V_{ds}}} \sum_k^{N_{V_{gs}}-1} \left((\Delta I_{\text{true}}^{(i,j,k)} - \Delta I_{\text{pred}}^{(i,j,k)})^2 + (\Delta \log_{10} I_{\text{true}}^{(i,j,k)} - \Delta \log_{10} I_{\text{pred}}^{(i,j,k)})^2 \right) \quad (\text{S3})$$

$$L_{\Delta^2 I_d}^{(i)} = \frac{1}{2N_{V_{ds}}(N_{V_{gs}}-2)} \sum_j^{N_{V_{ds}}} \sum_k^{N_{V_{gs}}-2} \left((\Delta^2 I_{\text{true}}^{(i,j,k)} - \Delta^2 I_{\text{pred}}^{(i,j,k)})^2 + (\Delta^2 \log_{10} I_{\text{true}}^{(i,j,k)} - \Delta^2 \log_{10} I_{\text{pred}}^{(i,j,k)})^2 \right) \quad (\text{S4})$$

where $N_{V_{ds}}$ and $N_{V_{gs}}$ are the number of V_{ds} and V_{gs} values, respectively, and j and k denote the j^{th} V_{ds} and k^{th} V_{gs} value, respectively. Δ and Δ^2 denote first and second differences with respect to V_{gs} , e.g.,

$$\Delta I_{\text{true}}^{(i,j,k)} = I_{\text{true}}^{(i,j,k)} - I_{\text{true}}^{(i,j,k-1)} \quad (\text{S5})$$

$$\Delta^2 I_{\text{true}}^{(i,j,k)} = \Delta I_{\text{true}}^{(i,j,k)} - \Delta I_{\text{true}}^{(i,j,k-1)} \quad (\text{S6})$$

Bootstrapping studies

We use a bootstrapping approach in **Figures 4a,b** in the main text to understand how varying the training set size influences the neural network's performance when reverse-engineering two-dimensional transistors. For each bootstrapped simulation, we build smaller training subsets by randomly selecting the specified number of devices from the original I_d - V_{gs} simulations. Afterwards, we initialize the forward and inverse models with random weights using the Glorot uniform initializer as implemented in Tensorflow, and carry out the training scheme using these smaller training sets.

R^2 calculations

Throughout the main text and supplementary information, we report individual R^2 values to measure the goodness of fit between data sets containing multiple baseline truths and predictions. A conventional R^2 that summarizes multiple data sets is not typically well defined. Here, for a set of N curves, we calculate the individual R^2 for every curve and then take the average of these values. For our I_d - V_{gs} curves, we include both the R^2 in linear space (i.e., as normally calculated) and R^2 in logarithmic space (i.e., transforming both the baseline truth and predicted I_d by taking their base 10 logarithm and then calculating the R^2 with these transformed values) in the above sum. These R^2 values are calculated on baseline and predicted I_d - V_{gs} curves after interpolating them onto 32 evenly spaced V_{gs} points and after imposing noise floor mapping, as described in the ‘‘interpolation’’ and ‘‘noise floor’’ procedures earlier in this section.

Supplementary Section 5: Details for the forward neural network

Here, we discuss the *forward neural network* (architecture in **Supplementary Figure S2a**) to predict I_d - V_{gs} curves from the model parameters in **Table 1**. In essence, this neural network approximates the original physics-based TCAD solver or, equivalently, it approximates M_{forward} in **Eq. (1)**. We emphasize that the forward neural network should not be confused with the *inverse neural network* that we use to reverse-engineer model parameters; the forward neural network is a surrogate model that (i) provides an augmented data set for pre-training our inverse neural network and (ii) is called when evaluating the loss function of our inverse neural network using a tandem approach (as in **Figure 3b** in the main text).

After scaling all data, we train the forward neural network to output I_d - V_{gs} curves with V_{gs} values evenly spaced from -6 to +50 V (see **Supplementary Section 4** for scaling and training procedures). The network outputs I_d - V_{gs} curves at $V_{ds} = 0.1$ and 1.0 V, in both linear and logarithmic space, yielding four separate curves. Although predicting both I_d and $\log_{10}(I_d)$ explicitly may seem redundant, we do so because the hyperbolic tangent activation functions in the network's output layer have range (-1, 1) and hence cannot easily predict outputs that span multiple orders of magnitude. Thus, we explicitly output $\log_{10}(I_d)$ to ensure we can accurately predict the off-state current, which tends to be many orders of magnitude smaller than the on-state current.

Forward neural network loss function

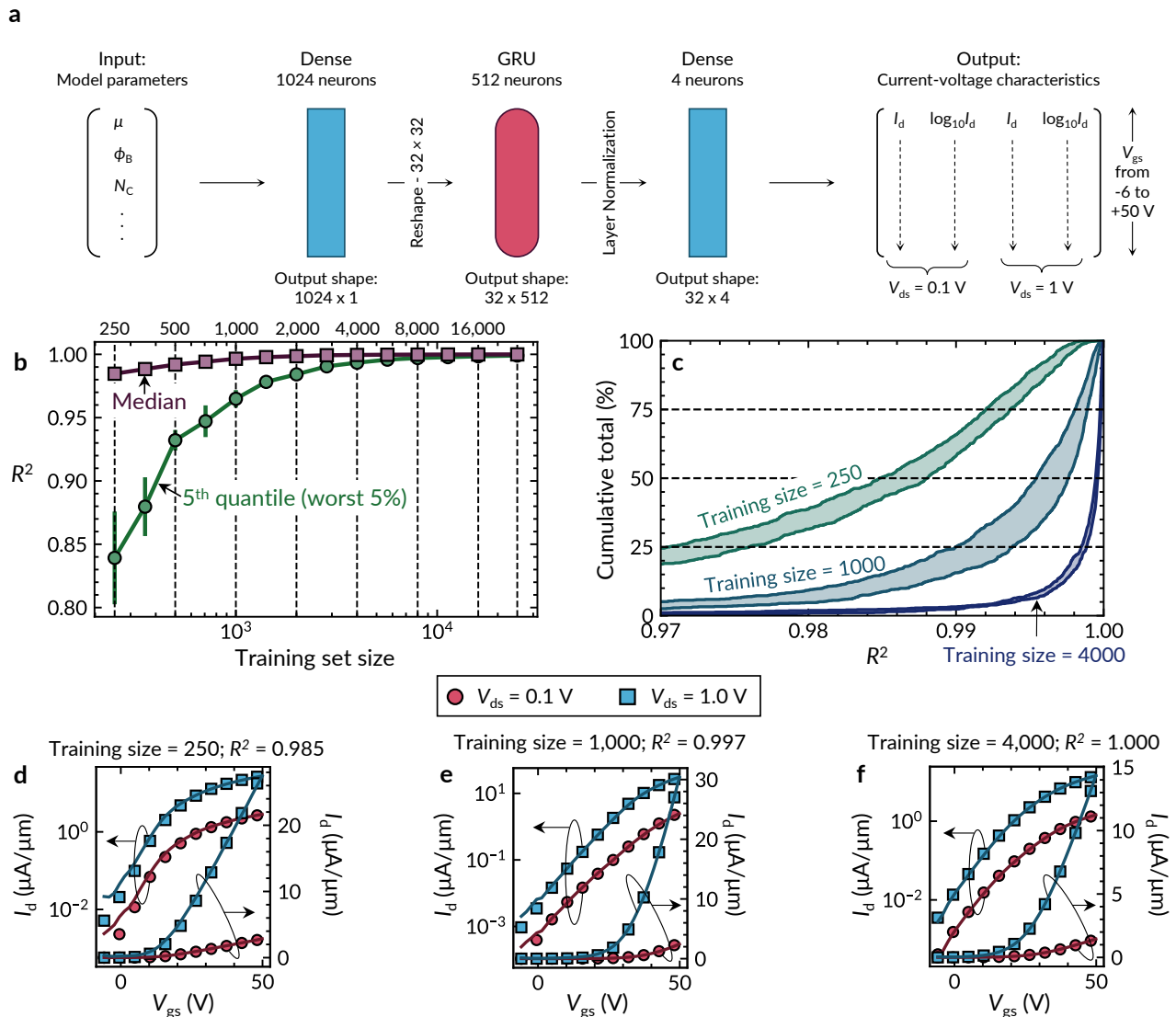
We use the loss function shown in **Eq. (S7)** when training the forward neural network. Here, we aim to ensure that the forward neural network predicts both the linear and $\log_{10}I_d$ values, along with the slopes and curvatures of the linear and $\log_{10}I_d$ - V_{gs} curves, across all V_{ds} values.

$$L_{\text{forward}} = \frac{1}{N_{\text{devices}}} \sum_i^{N_{\text{devices}}} \left(L_{\text{forward}}^{I_d^{(i)}} + L_{\text{forward}}^{\Delta I_d^{(i)}} + L_{\text{forward}}^{\Delta^2 I_d^{(i)}} \right) \quad (\text{S7})$$

Here, N_{devices} is the number of devices in the training set and i denotes the i^{th} device. Other terms in **Eq. (S7)** quantify the error in the I_d - V_{gs} measurements, along with errors in their slopes and curvatures, and are defined in **Eqs. (S2) to (S4)**.

Forward neural network performance

Because physics-based (TCAD) I_d - V_{gs} training data are computationally expensive, we wish to obtain high quality fits using as little training data as possible. Thus, we assess the forward network's performance vs. the number of devices included in training set using the bootstrap procedure described in **Supplemental Section 1**. Here, we find that for all training set sizes considered, our forward neural network can achieve a median $R^2 \geq 0.98$ on the test set (**Supplementary Figure S2b**), indicating a good match between the original simulated current and the approximation from the forward neural network. We are also interested in the network's performance across the vast majority of the test set; thus, we plot the 5th quantile R^2 (i.e., the R^2 corresponding to the worst 5% of fits) on the same axes, and we plot sample cumulative histograms of R^2 for different training set sizes in **Supplementary Figure S2c**. We find that the worst 5% of the fits still match well when the training set contains at least ~ 500 devices, for which we achieve a 5th quantile $R^2 \approx 0.94$. We show sample fits corresponding to the median R^2 after training on 250, 1,000, and 4,000 devices in **Supplementary Figures S2d-f** to confirm agreement between the original physics-based simulation and the network's predicted I_d .

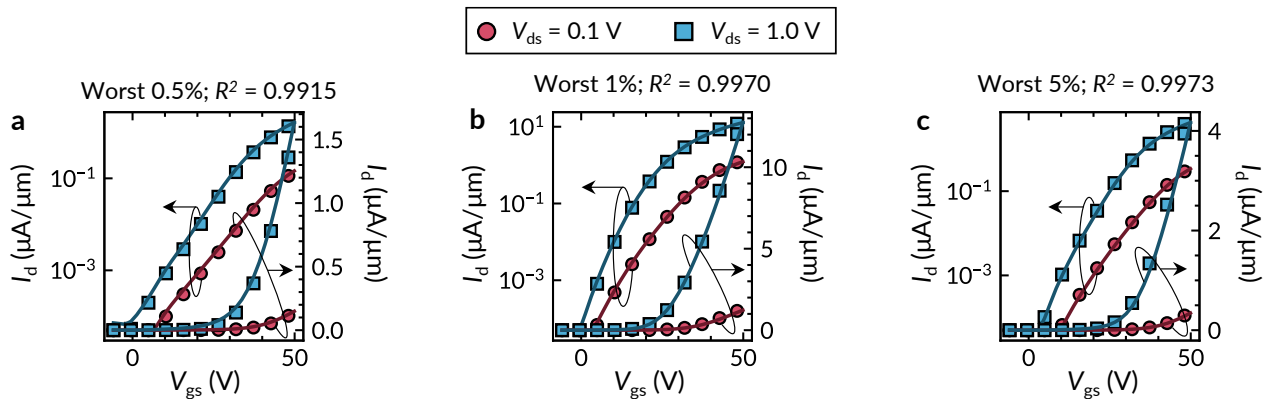


Supplementary Figure S2: Performance of the forward neural network used as a surrogate model. (a) The architecture of the neural network used to approximate the physics-based current model (“the forward neural network”). Dense layers use the hyperbolic tangent (\tanh) activation function. The gated recurrent unit (GRU) layer uses \tanh for its activation function and sigmoid for its recurrent activation function. (b) Median and 5th quantile (i.e., worst 5%) R^2 fits between the I_d calculated from the physics-based simulation and estimated by the forward neural network vs. the number of devices in the training set. Model fits were evaluated using a test set of 1,000 devices that were unseen by the model during training and network optimization. Error bars show standard deviation across five bootstrap tests (see **Supplementary Section 1** for details); error bars are often extremely small and hence are not always visible. (c) Cumulative R^2 fits for various training set sizes, where shaded regions show the range for the cumulative R^2 across the three bootstrapped tests. Current vs. gate-to-source voltage plots corresponding to the median R^2 fits after training on (d) 250 devices, (e) 1,000 devices, and (f) 4,000 devices (each plotted for the worst-performing bootstrapped network). Note that each device shown is different, because they are generated from a distribution of input parameters as listed in Table I. Symbols: original physics-based simulations; lines: neural network predictions. The data are shown on both logarithmic (left) and linear axes (right), at $V_{ds} = 0.1$ V (red symbols) and 1.0 V (blue symbols).

To assess the performance of the inverse neural network on the Sentaurus-simulated test set in **Figure 4** of the main text and during our ablation study in **Supplemental Section S3**, we compare the original I_d - V_{gs} curves to those obtained using the reverse-engineered parameters. To estimate the reverse-engineered I_d - V_{gs} curves, we take these extracted parameters input them into a well-trained forward neural network. This forward network was trained on all 25,000 devices in our original physics-based training set and followed the same training

procedure as described in **Supplementary Section 4**, with additional epochs and annealing steps to further minimize errors.

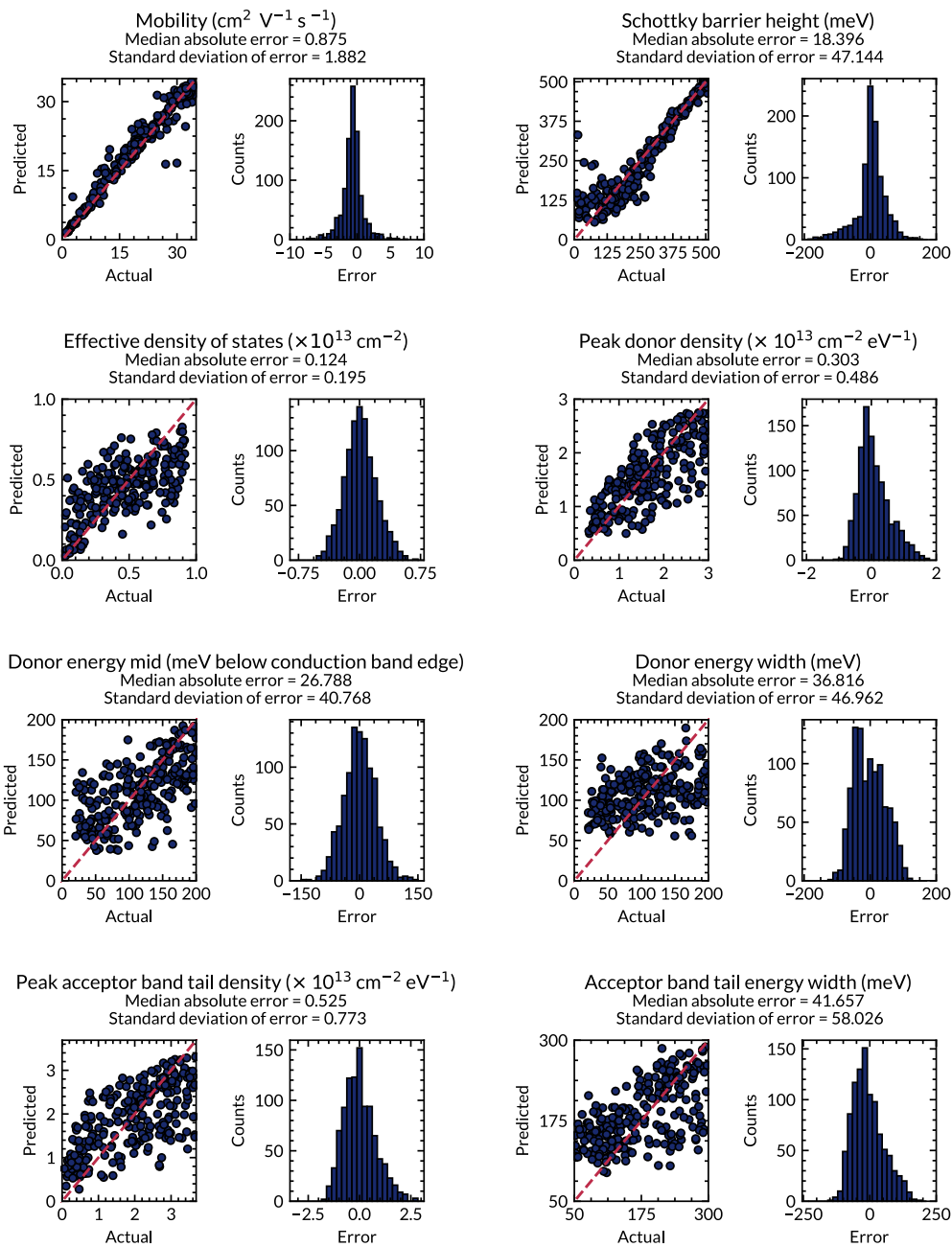
We test this well-trained forward network on the same test set of 1,000 devices and find that it reproduces the original Sentaurus-simulated I_d - V_{gs} characteristics exceptionally well: as shown in **Supplementary Figure S3**, this forward neural network achieves a 0.5th quantile, 1st quantile, and 2.5th quantile (i.e., worst 0.5%, worst 1%, and worst 2.5%) R^2 fit of 0.9915, 0.9970, and 0.9973, respectively, validating the use of this method for estimating R^2 .



Supplementary Figure S3: Performance of the well-trained forward neural network used to estimate R^2 in Figure 4 of the main text. Current vs. gate-to-source voltage plots of the worst 0.5%, 1%, and 2.5% R^2 sets obtained when testing the well-trained forward neural network on the Sentaurus-simulated test set. Even for these pessimistic scenarios, we find high $R^2 > 0.99$ across nearly all of the test set. Symbols: original physics-based simulations; lines: neural network predictions. The data are shown on both logarithmic (left) and linear axes (right), at $V_{ds} = 0.1 \text{ V}$ (red symbols) and 1.0 V (blue symbols).

Supplementary Section 6: Complete parameter extractions

Below, we show the actual vs. predicted values and corresponding error histograms for the eight model parameters from **Table 1** in the main text. We extract these parameters for the test set of 1,000 Sentaurus-simulated devices using the same inverse neural network as used in **Figures 4c-e and g,h** in the main text (i.e., this neural network was trained using 500 devices included in the main physics-based training set). To avoid cluttering plots of actual vs. predicted data, we plot only 250 out of 1,000 points from the test set when plotting actual vs. predicted values. The median absolute errors and standard deviation of errors were calculated from the full 1,000 devices, and the histograms show data from all devices as well. All units for each plot, except for histogram counts, are as indicated in the titles. We truncate the x -axes of the histograms at $\pm 4 \times$ the standard deviation of error for clarity.

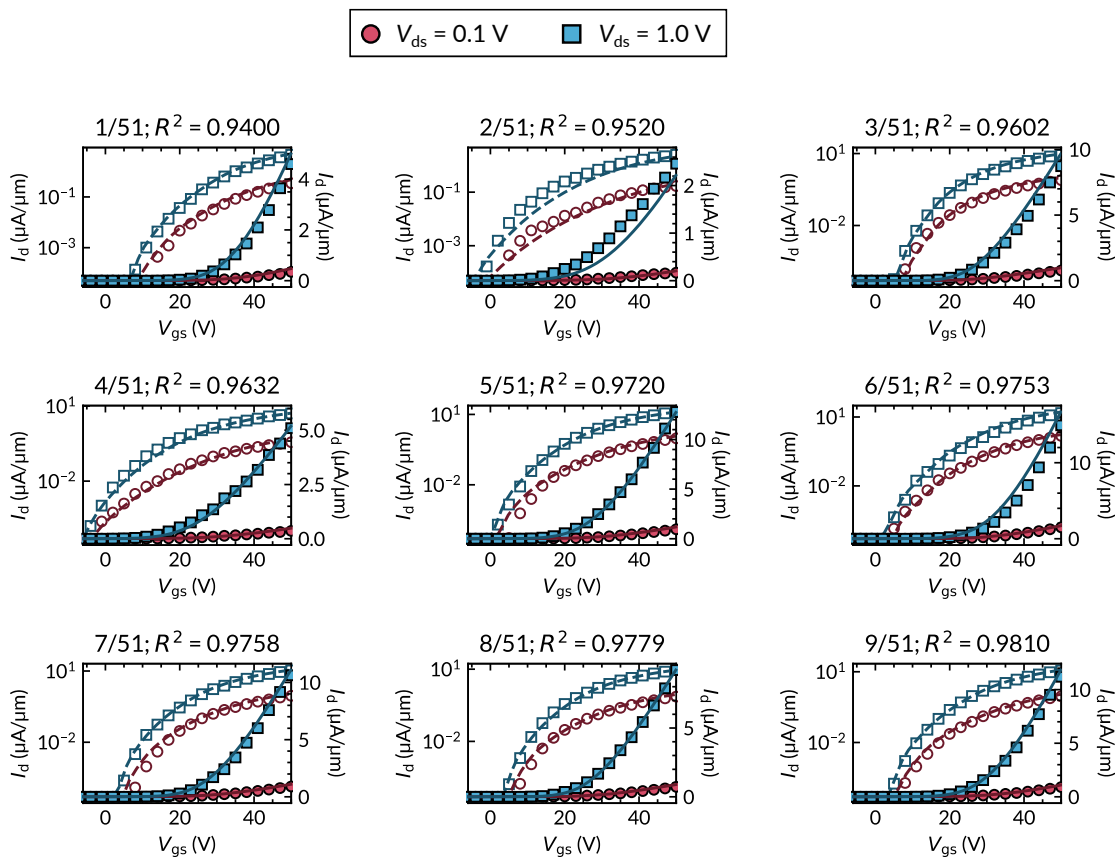


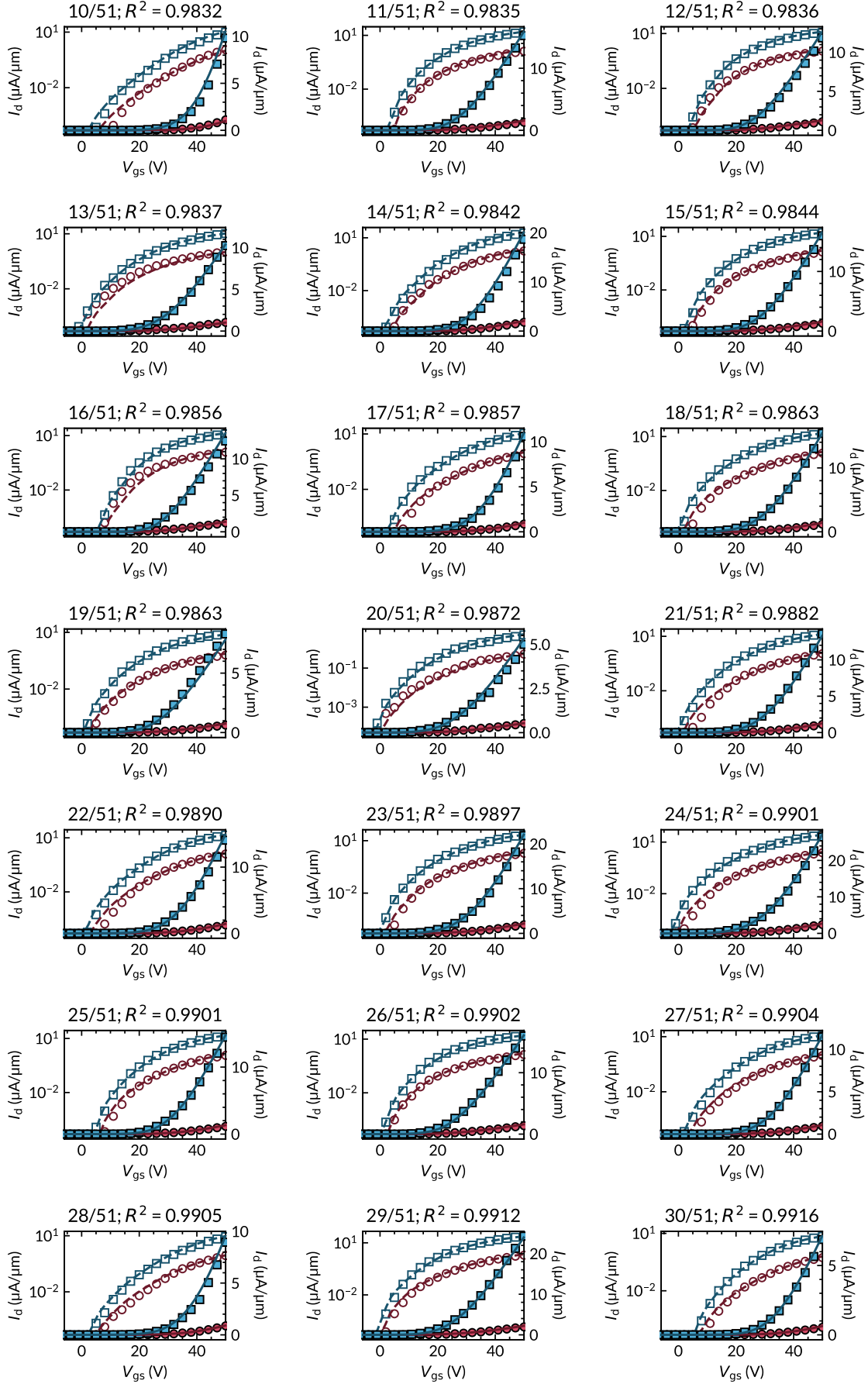
Supplementary Section 7: Experimental details and fits for all experimental devices

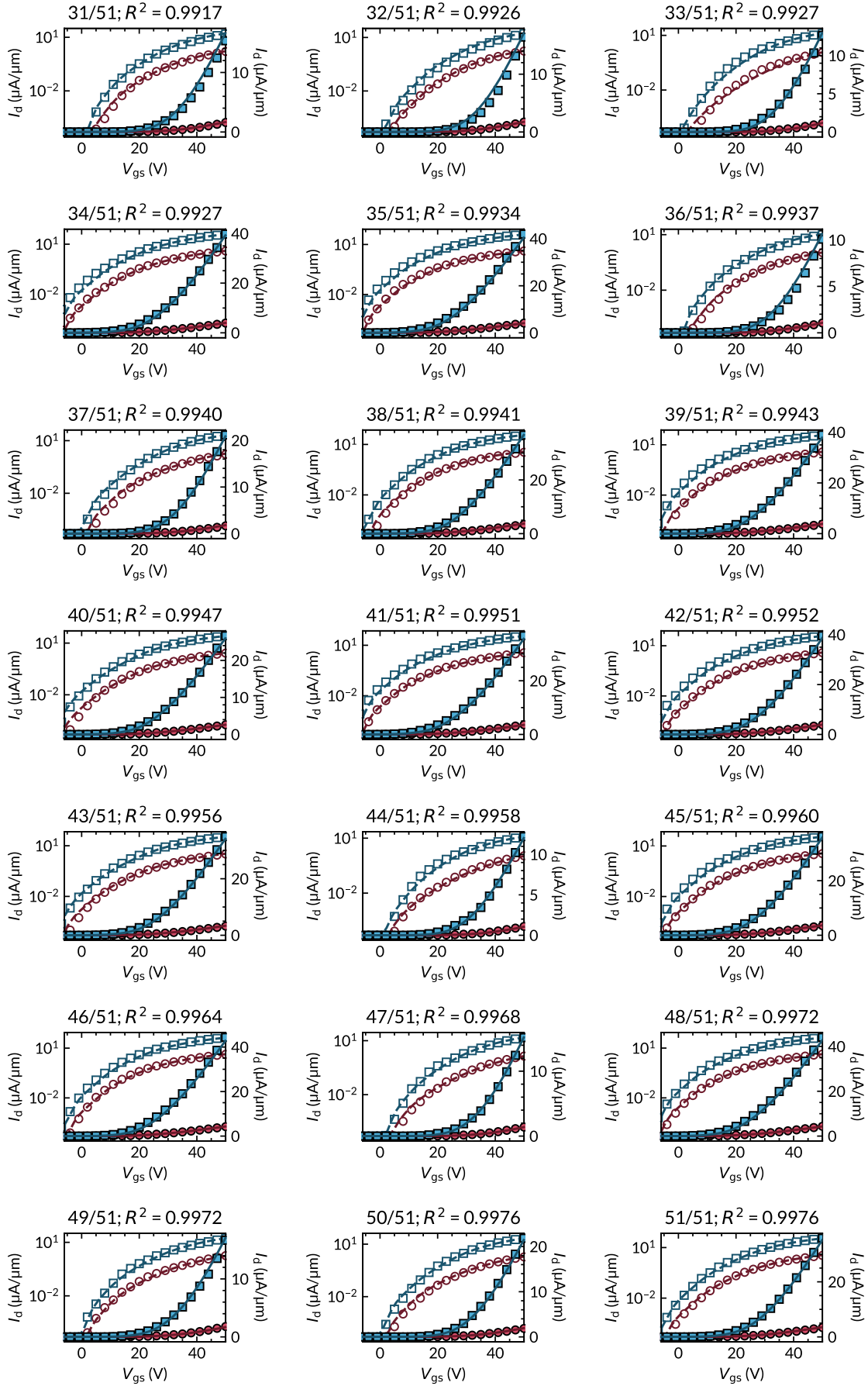
Monolayer WS₂ was grown by hybrid metal-organic chemical vapor deposition and was wet-transferred onto 100 nm SiO₂/p⁺⁺ Si, which served as the back-gate. Polystyrene was spin-coated on top of the WS₂ and then transferred in deionized water onto the target substrate (SiO₂/Si). Polystyrene was then removed using toluene. Electron-beam lithography was employed for each lithography step. First, large probing pads (Ti/Pt 2/20 nm) were patterned and deposited by electron beam evaporation via lift-off. Channel definition was done using xenon difluoride etching and the contacts were patterned for liftoff. Ni/Au contacts were evaporated by electron beam at $\sim 10^{-8}$ Torr. The channel and contact lengths of all devices were 500 nm and 1.5 μm , respectively. The devices were measured in a Janis ST-100 probe station at $\sim 10^{-4}$ Torr using a Keithley 4200 semiconductor parameter analyzer. These devices and measurements were described in a previous work.²⁰

Experimental devices were fabricated across three separate chips. We include all measured working devices in our test set, except for one device that could not achieve an on-state current $> 1 \mu\text{A}/\mu\text{m}$ at $V_{\text{ds}} = 1 \text{ V}$, leaving a total of 51 devices in our test set. Experimentally, we measure both forward and backward sweeps for each device using a V_{gs} range of $\pm 60 \text{ V}$; in this work, we use only the forward sweeps and restrict V_{gs} from -6 to +50 V for the reverse-engineering process described in the main text.

Below, we show fits across the experimental test set of 51 monolayer WS₂ transistors, ordered by ascending R^2 . We title each plot with the number of the device (ordered by the quality of the fit; 1/51 indicates the worst R^2 fit and 51/51 indicates the best R^2 fit). Filled markers and solid lines show the data on the linear scale (right) y-axis, and hollow markers and dashed lines show the data on the logarithmic scale (left) y-axis.







Supplementary Section 8: Details for high electron mobility transistor simulations

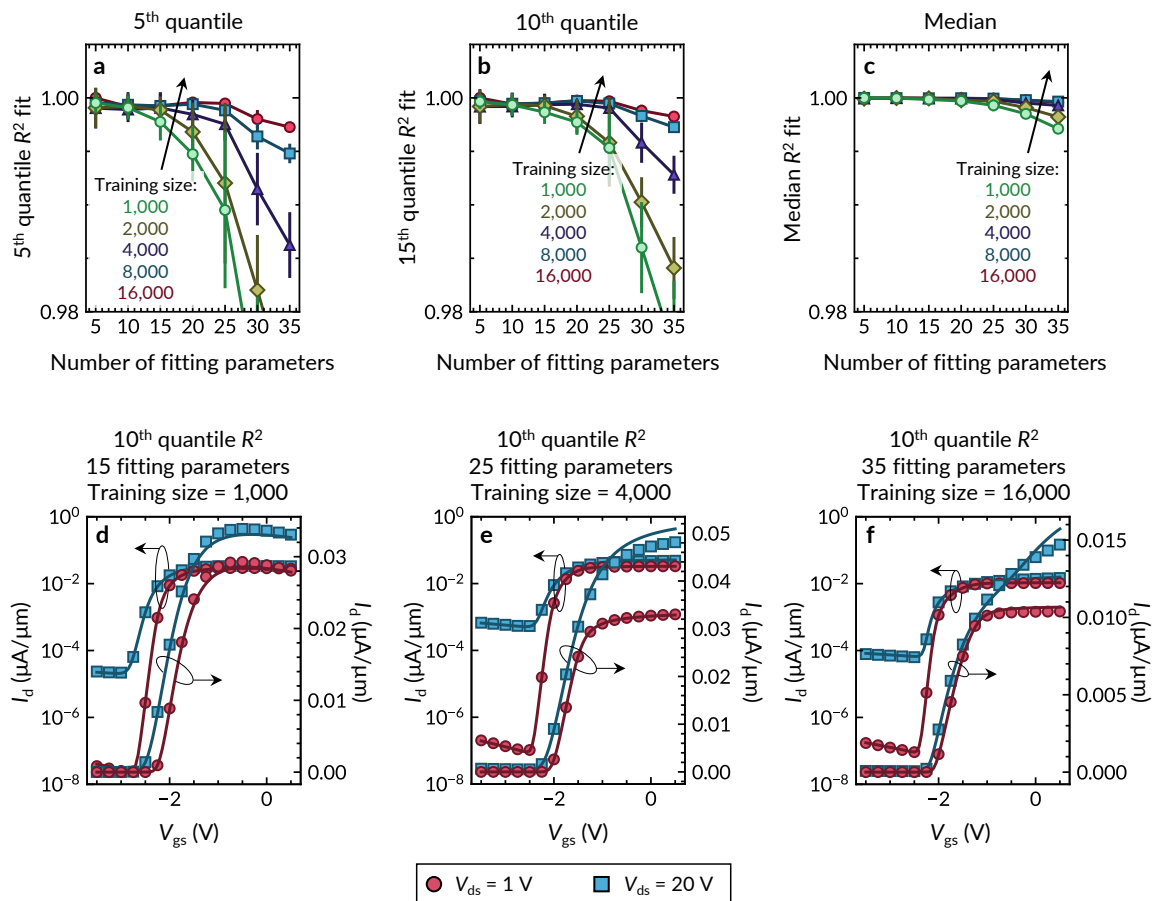
We use the fitting parameters and ranges shown in **Supplementary Table S1** for high-electron-mobility (HEMT) transistors with 150 nm channel lengths. We build our training/test sets from the ASM-HEMT compact model,²¹ and we pre-process in the same way as for two-dimensional transistors. Our training and test data sets consist of I_d - V_{gs} curves from $V_{gs} = -3.5$ to 0.5 V (evenly spaced across 32 values) at fixed drain biases of $V_{ds} = -1, 0.1, 1, 5, 10, 15,$ and 20 V. All neural network architectures are similar as for two-dimensional transistors, except that the forward neural network uses 512 and 256 neurons in its first dense layer and its gated recurrent unit (GRU) layer, respectively, and the number of neurons in the input and output layers are updated to accommodate the number of fitting parameters and V_{ds} values. Here, we wish to understand the impact of increasing the number of fitting parameters on accuracy of the inverse design procedure. Thus, we bootstrap not only the training data, but also the fitting parameters themselves.

When varying the number of fitting parameters used, we select the parameters that we vary at random from **Supplementary Table S1**; all other parameters are assigned default values at random from their respective ranges. This parameter set is very similar to that used in a previous work,²² with the ranges of some parameters having been expanded. We note that different fitting parameters could be easier or more difficult to fit compared to others. Therefore, for each of our five bootstrapped runs, we always progressively add additional fitting parameters. For example, in a bootstrap run, we begin by fitting 5 randomly selected parameters. When we fit 10 parameters, we select 5 additional parameters to vary alongside the first 5. When we fit 15 parameters, we select 5 additional parameters to vary alongside the first 10, and so on. For the next bootstrap run, we pick 5 new random fitting parameters and begin this process anew.

Parameter name	Range	Parameter name	Range
cdscd	0.01 – 0.15	rnjgd	15 – 30
eta0	0.01 – 0.1	rnjgs	5 – 15
delta	2 – 5	rsc	$10^{-5} - 1.5 \times 10^{-3}$
gdsmin*	$10^{-12} - 10^{-6}$	rth0	15 – 45
igddio	7.5 – 15	thesat	1 – 4
igsdio	2.5 – 10	u0	0.15 – 0.3
imin*	$10^{-15} - 10^{-12}$	u0accd	0.05 – 0.25
lambda	$10^{-4} - 5 \times 10^{-3}$	u0accs	0.05 – 0.25
mexpaccs	1 – 5	ua	$10^{-8} - 5 \times 10^{-7}$
mexpaccd	1 – 5	ub*	$10^{-21} - 10^{-15}$
nfactor	0.2 – 0.5	ute	-1 – -0.1
njgd	2.5 – 20	uted	-17.5 – -5
njgs	2.5 – 20	utes	-17.5 – -5
ns0accd*	$5 \times 10^{15} - 5 \times 10^{20}$	vdscale	2 – 6
ns0accs*	$5 \times 10^{15} - 5 \times 10^{20}$	voff	-2.1 – -1.9
rdc	$10^{-4} - 1.5 \times 10^{-3}$	vsat	$1.5 \times 10^6 - 2.5 \times 10^6$
rigddio	$10^{-8} - 10^{-7}$	vsataccs	$10^4 - 1.5 \times 10^5$
rigsdio	$10^{-8} - 10^{-7}$		

Supplementary Table S1: Fitting parameters and ranges across which they vary for the ASM-HEMT compact model simulations. The parameters and ranges across which they vary are very similar to those in a previous work²², with some ranges expanded (parameters not listed here take on the default values from this same reference). All parameter names and units are identical to those in the ASM-HEMT model. All fitting parameters were sampled uniformly across their respective ranges. A superscripted asterisk (*) after the parameter name denotes that this sampling was performed in logarithmic (base 10) space, e.g., for a parameter with lower and upper bounds A and B , we drew a random number c sampled uniformly between $\log_{10}A$ and $\log_{10}B$ and assigned the parameter a value $y = 10^c$.

We plot the 5th quantile (worst 5%), 10th quantile (worst 10%), and median R^2 fit as functions of the number of fitting parameters in **Supplementary Figure S4a-c** for various training size sets. Each test set contains sets of I_d - V_{gs} curves from 1,000 HEMTs that were unseen by the neural network during training and optimization. Here, we find that increasing the number of fitting parameters makes the extraction process more error-prone if the size of the training set remains constant. This is an unsurprising consequence of the “curse of dimensionality,”²³ since the available parameter space grows exponentially as the number of fitting parameters increases, making it increasingly difficult for the neural network to fit multiple parameters simultaneously. However, as we increase the size of our training sets, we find that we can somewhat compensate for this added complexity – for example, from **Supplementary Figure S4b**, we observe that when fitting 15 parameters simultaneously, training our neural networks on 1,000 devices in our training set yields a 10th quantile $R^2 > 0.995$ on the test set. We achieve a similar R^2 when fitting 25 and 35 parameters after training on 4,000 and 16,000 devices, respectively (sample fits shown in **Supplementary Figures S4d-f**). In other words, within this range, we must roughly quadruple the size of the training set for every 10 additional fitting parameters to maintain the same level of accuracy.



Supplementary Figure S4: neural network performance vs. complexity of fitted models. Plots of (a) the 5th quantile R^2 fit, (b) the 10th quantile R^2 fit, and (c) the median R^2 fit plotted vs. the number of fitting parameters in the ASM-HEMT compact model. We show curves of the R^2 fit vs. number of fitting parameters as level curves for each training size tested. Markers and error bars show the means and standard deviations of the R^2 fit for five bootstrapped runs. We truncate the y-axis at $R^2 = 0.98$ to avoid overcrowding the plot. Panels (d-f) show the fits corresponding to the 10th quantile (worst 10%) R^2 from a bootstrapped model when fitting 15, 25, and 35 parameters simultaneously after training on data from 1,000, 4,000, and 16,000 devices, respectively. In all panels, we calculate R^2 using the procedure described in **Supplementary Section 4** across all V_{ds} values used; in panels d-f, we plot I_d - V_{gs} curves at only $V_{ds} = 1$ and 20 V to avoid cluttering the plots.

Supplementary References

- 1 Synopsys, Inc. Sentaurus Device Manual. (2017).
- 2 Liu, X., Choi, M. S., Hwang, E., Yoo, W. J. & Sun, J. Fermi Level Pinning Dependent 2D Semiconductor Devices: Challenges and Prospects. *Advanced Materials* **34**, 2108425, doi:<https://doi.org/10.1002/adma.202108425> (2022).
- 3 Bennett, R. K. A., Hoang, L., Cremers, C., Mannix, A. J. & Pop, E. Mobility and threshold voltage extraction in transistors with gate-voltage-dependent contact resistance. *npj 2D Materials and Applications* **9**, 13, doi:10.1038/s41699-024-00506-4 (2025).
- 4 Roy, S. & Bermel, P. Electronic and optical properties of ultra-thin 2D tungsten disulfide for photovoltaic applications. *Solar Energy Materials and Solar Cells* **174**, 370-379, doi:<https://doi.org/10.1016/j.solmat.2017.09.011> (2018).
- 5 Jo, S., Ubrig, N., Berger, H., Kuzmenko, A. B. & Morpurgo, A. F. Mono- and Bilayer WS₂ Light-Emitting Transistors. *Nano Letters* **14**, 2019-2025, doi:10.1021/nl500171v (2014).
- 6 Falin, A. *et al.* Mechanical Properties of Atomically Thin Tungsten Dichalcogenides: WS₂, WSe₂, and WTe₂. *ACS Nano* **15**, 2600-2610, doi:10.1021/acsnano.0c07430 (2021).
- 7 Klinkert, C. *et al.* 2-D Materials for Ultrascaled Field-Effect Transistors: One Hundred Candidates under the Ab Initio Microscope. *ACS Nano* **14**, 8605-8615, doi:10.1021/acsnano.0c02983 (2020).
- 8 Evans, S. R., Deylgat, E., Chen, E. & Vandenberghe, W. G. Image-force barrier lowering of Schottky barriers in two-dimensional materials as a function of metal contact angle. *Physical Review Applied* **20**, 044003, doi:10.1103/PhysRevApplied.20.044003 (2023).
- 9 Hoang, L. *et al.* Understanding the Impact of Contact-Induced Strain on the Electrical Performance of Monolayer WS₂ Transistors. *Nano Letters* **24**, 12768-12774, doi:10.1021/acs.nanolett.4c02616 (2024).
- 10 He, Z., Yang, H. & Young Kim, N. Device simulation study of multilayer MoS₂ Schottky barrier field-effect transistors. *Nanotechnology* **36**, 035701, doi:10.1088/1361-6528/ad823e (2025).
- 11 Zhao, Y. *et al.* Electrical spectroscopy of defect states and their hybridization in monolayer MoS₂. *Nature Communications* **14**, 44, doi:10.1038/s41467-022-35651-1 (2023).
- 12 Jana, K. *et al.* in *2024 International Conference on Simulation of Semiconductor Processes and Devices (SISPAD)*. 01-04.
- 13 Wang, X. & Dodabalapur, A. Carrier Velocity in Amorphous Metal–Oxide–Semiconductor Transistors. *IEEE Transactions on Electron Devices* **68**, 125-131, doi:10.1109/TED.2020.3037890 (2021).
- 14 Liu, Y., Zeng, J., Zhu, Z., Dong, X. & Deng, W. A physics-based compact model for MoS₂ field-effect transistors considering the band-tail effect and contact resistance. *Japanese Journal of Applied Physics* **59**, 104004, doi:10.35848/1347-4065/abb7e1 (2020).
- 15 Chiquito, A. J. *et al.* Back-to-back Schottky diodes: the generalization of the diode theory in analysis and extraction of electrical parameters of nanodevices. *Journal of Physics: Condensed Matter* **24**, 225303, doi:10.1088/0953-8984/24/22/225303 (2012).
- 16 Nasr, J. R., Schulman, D. S., Sebastian, A., Horn, M. W. & Das, S. Mobility Deception in Nanoscale Transistors: An Untold Contact Story. *Advanced Materials* **31**, 1806020, doi:<https://doi.org/10.1002/adma.201806020> (2019).
- 17 Bennett, R. K. A. Deep learning for transistor parameter extraction (GitHub repository). Available online: <https://github.com/RKABennett/deep-learning-for-transistor-parameter-extraction>.
- 18 Kingma, D. P. & Ba, J. Adam: A method for stochastic optimization. *arXiv*, doi:<https://doi.org/10.48550/arXiv.1412.6980> (2014).
- 19 Martín, A. *et al.* TensorFlow: Large-Scale Machine Learning on Heterogeneous Systems. (2015).
- 20 Zhang, Z. *et al.* Chemically Tailored Growth of 2D Semiconductors via Hybrid Metal–Organic Chemical Vapor Deposition. *ACS Nano* **18**, 25414-25424, doi:10.1021/acsnano.4c02164 (2024).
- 21 Dasgupta, A., Ghosh, S., Chauhan, Y. S. & Khandelwal, S. in *2015 IEEE International Conference on Electron Devices and Solid-State Circuits (EDSSC)*. 495-498 (2015).
- 22 Martinez, R. P. *et al.* Compact Model Parameter Extraction via Derivative-Free Optimization. *IEEE Access* **12**, 123224-123235, doi:10.1109/ACCESS.2024.3453198 (2024).
- 23 Köppen, M. in *5th online world conference on soft computing in industrial applications (WSC5)*. 4-8 (2000).